How do earthquakes stop? Insights from a minimal model of frictional rupture

Fabian Barras[1], Kjetil Thøgersen[1], Einat Aharonov[1,2], François Renard[1,3]

[1]The Njord Centre, Departments of Geosciences and Physics, box 1048, University of Oslo, Blindern, 0316

Oslo, Norway

[2]Institute of Earth Sciences, The Hebrew University, Jerusalem, 91904, Israel

[3]ISTerre, Univ. Grenoble Alpes, Grenoble INP, Univ. Savoie Mont Blanc, CNRS, IRD, Univ. Gustave

Eiffel, 38000, Grenoble, France

Key Points:

- A minimal model of frictional rupture describes large earthquake ruptures
- Two dimensionless parameters, $\bar{\tau}_k$ and $\bar{d}_c$, account for all known mechanisms of earthquake arrest
- The model illuminates the different energy balance that drives crack-like and pulse-like ruptures
- The model produces asymmetric fault slip profiles, stress drop independence of the rupture size, and back-propagating ruptures

Corresponding author: Fabian Barras, `fabian.barras@mn.uio.no`

Abstract

The question "what arrests an earthquake rupture?" sits at the heart of any potential prediction of earthquake magnitude. Here, we use a one-dimensional, thin-elastic-strip, minimal model, to illuminate the basic physical parameters that control the arrest of large ruptures. The generic formulation of the model allows for wrapping various earthquake arrest scenarios into the variations of two dimensionless variables $\bar{\tau}_k$ (initial pre-stress on the fault) and $\bar{d}_c$ (fracture energy), valid for both in-plane and antiplane shear loading. Our continuum model is equivalent to the standard Burridge-Knopoff model, with an added characteristic length scale, H, that corresponds to either the thickness of the damage zone for strike-slip faults or to the thickness of the downward moving plate for subduction settings. We simulate the propagation and arrest of frictional ruptures and derive closed-form expressions to predict rupture arrest under different conditions. Our generic model illuminates the different energy budget that mediates crack- and pulse-like rupture propagation and arrest. It provides additional predictions such as generic stable pulse-like rupture solutions, stress drop independence of the rupture size, the existence of back-propagating fronts, and predicts that asymmetric slip profiles arise under certain pre-stress conditions. These diverse features occur also in natural earthquakes, and the fact that they can all be predicted by a single minimal framework is encouraging and pave the way for future developments of this model.

Plain Language Summary

Untangling the dynamics that governs the propagation and arrest of earthquakes is still challenging, mainly because of the few constraints available on the fault zone geometry, the constitutive properties of fault materials, as well as fault rheology during the rupture event. The present study aims at formulating a model containing a minimal number of free parameters to describe the dynamics of large earthquakes. Despite its simplicity, this minimal model is able to reproduce several salient features of natural earthquakes that are still debated (e.g. various arrest scenarios, stable pulse-like rupture, back-propagating front, asymmetric slip profiles). We demonstrate how the proposed model can be used to simulate the propagation and arrest of large earthquakes, which are controlled by local variations of shear stress and material properties on the fault. With this simple and generic description, the proposed model could be readily extended to account for additional processes controlling the dynamics of large earthquakes.

1 Introduction

Frictional rupture, the process by which a dynamic rupture propagates along a pre-existing interface, has been proposed to control many geological processes, including earthquakes, landslides, glacier instabilities, and snow avalanches (e.g., Palmer and Rice (1973); Scholz (1998); Viesca and Rice (2012); Gabriel et al. (2012); Scholz (2019); Thøgersen, Gilbert, et al. (2019); Weng and Ampuero (2019); Agliardi et al. (2020); Trottet et al. (2022)). In these systems, a rupture nucleates at a given location along an interface, accelerates to a maximum velocity, and then decelerates until final arrest. The entire process is controlled by heterogeneities of the initial (normal and shear) stress conditions, roughness of the interface, and material properties along the interface and in the surrounding volume.

During frictional rupture, initial elastic strain energy stored in the volume around the interface is transformed into several components that involve 1) a transfer of elastic strain energy between different locations along the interface and in the volume around it; 2) near-fault dissipation accounting for co-seismic fracture and damage of the rock as well as frictional dissipation and heat production during slip; 3) emission of elastic waves (i.e. seismicity).

The arrest of frictional rupture can be predicted at the scale of laboratory experiments when rupture arises along the interface between two elastic blocks pressed in frictional contact (e.g. Kammer et al. (2015); Bayart et al. (2016); Ke et al. (2018)). In this setup, the prediction builds upon the analogy to brittle shear fracture and requires to know an equivalent fracture energy of the frictional plane, which varies with the normal stress. Upscaling these predictions to natural earthquakes remains out of reach due to the complexity of the fault geometry (e.g., roughness, bends, segmentation), of the fault zone rheology (e.g. damage zone), as well as due to the difficulty in estimating and measuring how the various components of the earthquake energy budget interplay in transforming and consuming the initial elastic strain energy available before rupture propagation (e.g., Abercrombie and Rice (2005); Tinti et al. (2005); Barras et al. (2020); Lambert and Lapusta (2020); Brener and Bouchbinder (2021); Paglialunga et al. (2021); Ke et al. (2022)). Prediction of rupture arrest is made even more difficult by the fact that earthquake propagation can arise under two distinct rupture modes; either crack-like or pulse-like (e.g., Scholz (2019); Lambert et al. (2021)). In conventional crack-like ruptures, also called circular cracks, all points within the growing ruptured area keep sliding un-

til arrest (Burridge & Halliday, 1971; Madariaga, 1976; Kostrov & Das, 1988). Conversely, for pulse-like ruptures, a rupture front propagates along the interface and heals behind it, such that every point of the interface will accelerate, slip and arrest at different times (Heaton, 1990).

This complexity explains why a full comprehensive description of the conditions governing the arrest of an earthquake, and therefore its final size and magnitude, is still missing. Several scenarios of rupture arrest have been proposed in the literature and could be divided into two main categories. On the one hand, a rupture may stop because a local geometrical or mechanical heterogeneity, also called barrier, prevents further propagation (Das & Aki, 1977; Aki, 1979). On natural faults, a barrier could be related to fault segmentation (Sibson, 1985; Sibson & Das, 1986; Wesnousky, 1988; Harris & Day, 1999), to the fact that, near fault tip, rocks may be stronger and require more energy to break (e.g. concept of fault maturity, see Perrin et al. (2016)), or to variations in frictional properties (Marone & Scholz, 1988). On the other hand, a rupture may stop because of a non-local effect related to the preexisting stress along the sliding interface. For example, if a fault has been unloaded by a previous earthquake, the shear stress along the interface will be lower than for a fault that has not broken for a long period and that has been loaded by tectonic stress during that period. In this situation, a frictional rupture may arrest because of the depletion of available elastic strain energy along a section of the fault. In other words, the rupture stops because it "runs out of steam".

Here, we explore the dynamics governing the propagation and arrest of frictional rupture by using a one-dimensional elastodynamic model that contains only two parameters in its dimensionless form (Thøgersen et al., 2021). A similar approach reproduces some observations made on slow, subshear, and supershear earthquakes, such as the scaling between duration and moment (Thøgersen, Sveinsson, et al., 2019). This minimal model builds on the approximation of the earthquake dynamics existing at the later stage of the rupture once its size exceeds the width of the seismogenic zone. The resulting one-dimensional formulation, summarized in Section 2, considers a thin elastic strip in frictional contact along a preexisting interface (Fig. 1c), which may represent either a subduction setting (Fig. 1a) or a strike-slip fault (Fig. 1b) once the earthquake dynamics transition from *circular crack growth* towards the propagation of a *planar front*. Such transition is depicted by the successive dashed red lines in Fig. 1a-b and have been reported in numerical simulations (Weng & Ampuero, 2019; Day, 1982), as well as from

115   seismic inversion of natural earthquakes (Chen et al., 2022, 2020). The elastic strip is

116   defined by its thickness, H, and two elastic parameters, the first and second Lamé co-

117   efficients, λ and $\mathcal{G}$. H may represent the plate thickness (Fig. 1a) or the thickness of the

118   damage zone (Fig. 1b).

119   The model includes inertial effects in the direction of rupture propagation but ne-

120   glects them in the normal direction. Along the interface, sliding occurs according to a

121   friction law that either considers a sharp drop from static to dynamic friction (Amontons-

122   Coulomb model) or accounts for a weakening distance and associated fracture energy (slip-

123   weakening model). Rupture arrest is studied and discussed for these two friction mod-

124   els and two different rupture modes, crack versus pulse. Our approach is both numer-

125   ical (Section 3) and analytical, since the simplicity of our model allows for the reproduc-

126   tion of a wide range of rupture arrest scenarios and their description with analytical ex-

127   pressions (Section 4). Section 4 compares our one-dimensional continuum model with

128   the seminal discrete Burridge-Knopoff model for earthquakes (Burridge & Knopoff, 1967).

129   Using our minimal model, we present the boundary conditions that control the selection

130   of the rupture mode (either pulse-like or crack-like) and describe the substantial differ-

131   ence that exists between these two modes in terms of the rupture energy balance and

132   arrest conditions. The study concludes by highlighting how our one-dimensional frame-

133   work bridges different earthquake models proposed in the literature and by discussing

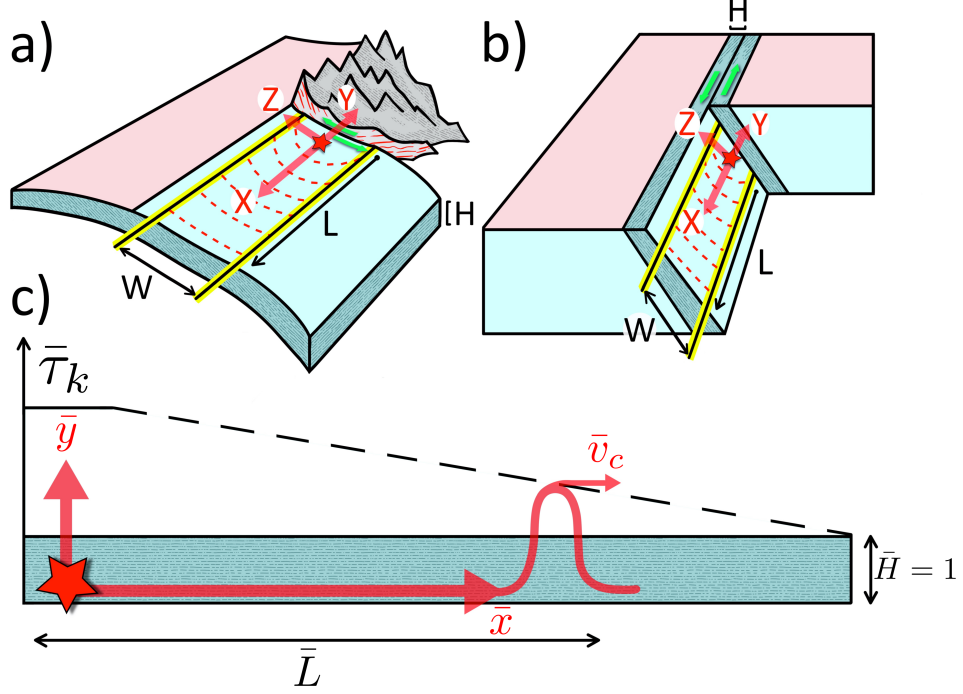134   its implications for earthquake arrest in natural fault zones (Section 5).

Figure 1. A minimal model to study frictional rupture arising along two types of plate boundaries, where loading is applied at a distance H from the fault. a) convergent (subduction zone or continental collision, H is the thickness of the down-moving plate), and b) transform fault (strike-slip, H is the thickness of the damage zone). In panels a) and b), the direction of plate motion is shown by a pair of green arrows. Cross-sections reveal the frictional interface between the two tectonic plates as well as the seismogenic zone of width W that hosts dynamic ruptures. Earthquake propagation is depicted by the successive red dashed lines, starting from the nucleation location shown by the red stars, and L is the rupture length. Initially, the earthquake grows as a *circular crack*. As the size of the rupture exceeds H and W, the earthquake propagates as a *planar front*. The profile of pre-stress, $\bar{\tau}_k$, is sketched in panel c) and has its peak in the nucleation zone set on the left of the domain. The propagation and arrest conditions are investigated in this study as the rupture propagates (rightwards) into a region less favorable to slip (lower pre-stress, higher frictional dissipation, barriers).

₁₃₅ ## 2 A one-dimensional minimal model of frictional rupture

The present study investigates rupture arrest using a minimal frictional rupture model that we developed in a previous study (Thøgersen et al., 2021). In this approach, the elastodynamic equations are reduced to a one-dimensional expression by assuming a block of finite height H in frictional contact along the plane $y = 0$, as presented in Figs. 1c and 2. The elastic fields are further taken constant along the z direction ($\partial_z u_i = 0$) during frictional ruptures that propagate along the x direction. Assuming that the rupture size L is always much larger than the system height ($L \gg H$), the elastodynamics can be solved in average over H to reduce momentum conservation into a one dimensional equation (Supplementary Information text S.1). The resulting one-dimensional equation is expressed here in dimensionless units of space $\bar{x}$ and time $\bar{t}$, with the dot accent denoting a time derivative:

$$\ddot{\bar{u}} = \frac{\partial^2 \bar{u}}{\partial \bar{x}^2} - \Gamma \bar{\gamma} \bar{u} + \bar{\tau}. \tag{1}$$

Γ is a binary operator being respectively equal to one if Eq. (1) describes a system with imposed-displacement boundary conditions at the top surface ($y = H$), or to zero if the system has imposed-stress at the top boundary. In the equation above, $\bar{u}(\bar{x}, \bar{t})$ is a scalar dimensionless displacement along the x-direction and $\bar{\tau}(\bar{x}, \bar{t})$ is a scalar dimensionless shear stress along the interface and defined as

$$\bar{\tau}(\bar{x}, \bar{t}) = \frac{\tau_0(\bar{x}) - \tau_f(\bar{x}, \bar{t})}{\sigma_n(\mu_s - \mu_k)}. \tag{2}$$

₁₃₆ Here, $\bar{\tau}(\bar{x}, \bar{t})$ lumps the initial shear stress acting on the top of the block before the rup-
₁₃₇ ture τ_0, the frictional stress at the interface τ_f, the normal stress σ_n, the static μ_s and
₁₃₈ kinematic μ_k friction coefficients. The static friction coefficient describes the magnitude
₁₃₉ of the shear stress that should be locally exceeded at the interface to initiate frictional
₁₄₀ sliding. The kinematic friction coefficient describes the residual frictional stress observed
₁₄₁ at the interface during sliding. More details about the boundary conditions are given in
₁₄₂ Section S.1 of the Supporting Information. The normal stress is assumed to be constant
₁₄₃ throughout the rupture, such that the model similarly applies to elastic-over-rigid and
₁₄₄ to symmetric frictional contact problems. The momentum equation, Eq. (1), equivalently
₁₄₅ applies to in-plane (mode II) and out-of-plane (mode III) shear loading configurations,
₁₄₆ as summarized in Table S1 that compiles the definitions of the dimensionless variables.

In its simplest form, the model contains only two free parameters: 1) a dimensionless ratio of elastic moduli $\bar{\gamma}$ defined in Table S1, and 2) a spatial variable referred to as

the dimensionless pre-stress in the manuscript

$$\bar{\tau}_k(\bar{x}) = \frac{\tau_0(\bar{x})/\sigma_n - \mu_k}{\mu_s - \mu_k}, \tag{3}$$

147   which corresponds to the value of $\bar{\tau}$ that will be observed once the frictional stress at the

148   interface reaches kinetic friction associated to positive slip velocity. The definition of $\bar{\tau}_k$

149   allows for lumping spatial variations of initial stress and frictional parameters into a sin-

150   gle variable. In the present study, we assume that variations of $\bar{\tau}_k$ results only from τ_0,

151   but spatial variations of the other parameters (σ_n, μ_s, μ_k) can similarly be translated

152   into a $\bar{\tau}_k(\bar{x})$ profile in the one-dimensional model with no loss of generality.

     In the dimensionless form used in the model, static friction is observed as long as

$$\bar{\tau}_f(\bar{x}, \bar{t}) = \bar{\tau}_k(\bar{x}) - \bar{\tau}(\bar{x}, \bar{t}) < 1, \tag{4}$$

153   where $\bar{\tau}_f$ is the dimensionless frictional stress, as detailed in the section S.1, Eq. (S.13).

154   Upon the onset of sliding, the frictional stress $\bar{\tau}_f(\bar{x}, \bar{t})$ locally drops from the static thresh-

155   old ($\bar{\tau}_f = 1$) to residual friction ($\bar{\tau}_f = 0$) following the trajectory prescribed by a fric-

156   tion law. In the remainder of the study, we focus on two generic friction laws and we re-

157   fer to Section 5 below for further discussions on how to relate more sophisticated fric-

158   tion laws to this minimal description. The simplest friction law assumes that the tran-

159   sition between static and kinematic friction is instantaneous upon sliding and requires

160   no additional parameter. In the rest of the study, it is referred to as *Amontons-Coulomb*

161   friction. Moreover, frictional weakening often comes with an energy dissipation on top

162   of residual friction that will be referred to as *breakdown work*, $\bar{W}_b$. A common and generic

163   description of this process assumes that frictional weakening between μ_s and μ_k devel-

164   ops linearly with slip between $\bar{u} = 0$ and some critical slip distance $\bar{u} = \bar{d}_c$. This fric-

165   tion law will be referred to as *slip-weakening* in the manuscript and introduces a third

166   free parameter $\bar{d}_c$, which directly relates to the interface *fracture energy* $\bar{G}_c = \bar{d}_c/2$. $\bar{G}_c$

167   corresponds to the total amount of breakdown work required to reach residual friction.

168   See section S.1 and equation (S.13) for more details on the non-dimensional descriptions

169   of Amontons-Coulomb and slip-weakening friction laws used in this paper.

170   **2.1 The crucial role of boundary conditions on the rupture style**

     Following the definitions above, $\bar{\tau}_k$ corresponds to the value of $\bar{\tau}$ in Eq. (1) observed

once the shear stress (or friction) at the interface reaches its residual level. Postulating

a steady-state solution and Amontons-Coulomb friction, Eq. (1) reduces to the follow-

ing ordinary differential equation within the rupture (i.e. within the sliding portion of the interface):

$$(\bar{v}_c^2 - 1)\frac{\partial^2 \bar{u}}{\partial \bar{\xi}^2} = -\Gamma\bar{\gamma}\bar{u}(\xi) + \bar{\tau}_k(\xi), \tag{5}$$

171   with $\bar{\xi} = \bar{x} - \bar{v}_c\bar{t}$ being a co-moving coordinate following the rupture (i.e. the position

172   of peak velocity) that moves at the propagation velocity $\bar{v}_c$.

173   Thøgersen et al. (2021) investigated steady-state rupture solutions governed by Eq.

174   (5) and revealed the crucial role of boundary conditions on the rupture style and its sta-

175   bility. For imposed-stress boundary condition ($\Gamma = 0$), the system promotes crack-like

176   rupture and no steady-state pulse solution exists. Pulse-like rupture can be produced

177   under the specific condition ($\bar{\tau}_k = 0$), which reduces Eq. (5) to a one-dimensional wave

178   equation. Such pulse solutions have no specific shape and are unstable, as a local per-

179   turbation in the stress or interface conditions $\delta\bar{\tau}_k$ either stops the pulse (if $\delta\bar{\tau}_k < 0$) or

180   expands it into a crack (if $\delta\bar{\tau}_k > 0$). Such unstable dynamics is reminiscent of the be-

181   havior of pulse-like ruptures between two semi-infinite elastic solids that have been re-

182   ported in the literature for different type of friction laws (Gabriel et al., 2012; Brener

183   et al., 2018; Brantut et al., 2019).

     Conversely, imposed-displacement boundary condition ($\Gamma = 1$) enables stable pulse solutions for $\bar{\tau}_k > 0$. Under uniform pre-stress conditions, the equation (5) allows a steady-state pulse solution with width $\bar{\omega}$ and the following slip profile:

$$\bar{u}(\bar{\xi}) = \frac{\bar{\tau}_k}{\bar{\gamma}}\Big(1 - \sin(\pi\bar{\xi}/\bar{\omega})\Big), \tag{6}$$

for $\bar{\xi} \in [-\bar{\omega}/2, \bar{\omega}/2]$. From the equation above, the final slip, $\bar{u}_p$, reached behind the steady-state pulse rupture corresponds to:

$$\bar{u}_p = 2\bar{\tau}_k/\bar{\gamma}. \tag{7}$$

184   Remarkably, this behavior is also in agreement with the stable pulse-like rupture that

185   was reported in previous works studying finite elastic domains, where reflected elastic

186   waves at the boundary interplay with the propagating rupture. This includes fault sys-

187   tem with a damage zone with more compliant elastic properties (Idini & Ampuero, 2020)

188   or earthquake rupture with a large aspect ratio (Weng & Ampuero, 2019). Interestingly,

189   train of stable steady-state pulses can be produced also at the interface between unbounded

190   elastic domains if an average slip velocity is imposed along the frictional plane instead

191   of controlling the far-field stress (Roch et al., 2022). In our model, this second type of

192   boundary condition ($\Gamma = 1$) corresponds then to large earthquake rupture, whose size

saturates two representative dimensions of the fault systems, as depicted in Fig. 1. Thøgersen et al. (2021) discusses in details the properties of slip pulses in our one-dimensional model.
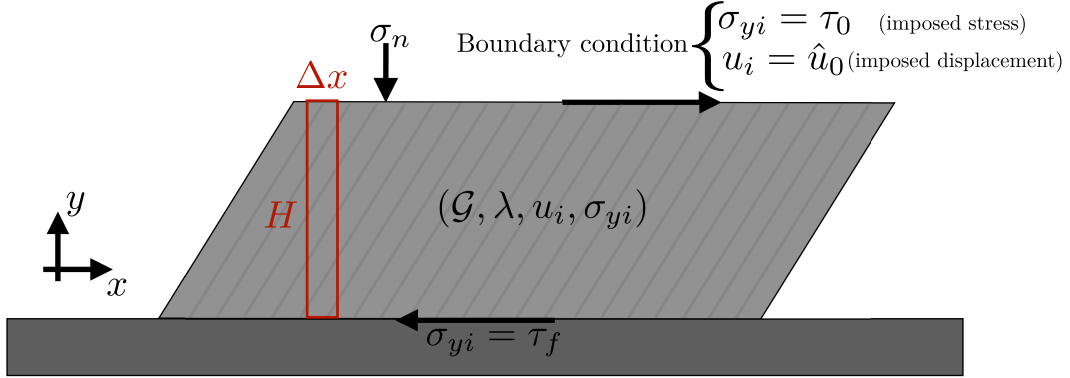

Figure 2. Sketch of the two-dimensional system that is integrated to obtain the one-dimensional equation of motion used in the manuscript. We model a thin elastic layer of thickness H with shear modulus $\mathcal{G}$ and the first Lamé coefficient λ. Two boundary conditions are considered on the top surface. At $y = H$ we apply either an imposed stress τ_0 or an imposed displacement $\hat{u}_0$. At $y = 0$, we apply a friction law. The system is integrated across the y-coordinate (red rectangle) to obtain a one-dimensional approximation. Modified from Thøgersen et al. (2021).

2.2 The arrest of frictional rupture in the one-dimensional model

The one-dimensional model (Eq. 1) used in the present study contains two free parameters for Amontons-Coulomb friction ($\bar{\gamma}$, $\bar{\tau}_k$) and an additional third parameter ($\bar{d}_c$) for slip-weakening friction. $\bar{\gamma}$ characterizes the elastic properties of the medium that are assumed to be macroscopically homogeneous and remain constant in the derivation of the model. Hence, a propagating rupture in the one-dimensional model can either be arrested by variations of $\bar{\tau}_k$ or $\bar{d}_c$. The former accounts for the level of shear stress existing in the system prior the rupture. A sharp reduction of $\bar{\tau}_k$ can stop a propagating rupture and corresponds to a *stress barrier*. Moreover, the initial finite amount of strain energy available in the surrounding bulk of thickness H scales as the square of τ_0 and is therefore proportional to $\bar{\tau}_k$. In the one-dimensional system, $\bar{\tau}_k$ describes the difference between external shear stress and the lowest value of frictional stress during sliding. If $\bar{\tau}_k$ is negative, this implies that the work injected by the external shear stress would be locally smaller than the frictional dissipation at residual frictional and, therefore, a fric-

tional rupture would absorb energy instead of releasing it. Hence, frictional ruptures in our one-dimensional model are energetically admissible only if somewhere along the interface

$$\bar{\tau}_k \geq 0. \tag{8}$$

196 Note that Eq. (8) is a necessary condition for frictional rupture in the one-dimensional
197 model but is not sufficient. It only guarantees rupture propagation once it has been nu-
198 cleated. A gradual decay of $\bar{\tau}_k$ as one moves away from the nucleation site can then lead
199 to the rupture arrest by a *depletion of available energy* in the system. Conversely, $\bar{d}_c$ de-
200 scribes the energy required to transform the interface shear conditions from static to kine-
201 matic friction. An increase in $\bar{d}_c$ can then arrest the rupture, which corresponds to a *frac-*
202 *ture energy barrier*. In the Sections 3 and 4, we simulate and study theoretically pulse-
203 and crack-like rupture arrest for these different arrest scenarios. Further in Section 5,
204 we discuss how variations of physical conditions along natural fault systems can be ex-
205 pressed in terms of spatial variations of $\bar{\tau}_k$ and $\bar{d}_c$.

206 ## 3 Numerical simulations of frictional rupture arrest

Here, Eq. (1) is solved numerically using a finite difference scheme with uniform grid size $\Delta \bar{x}$ and Euler-Cromer (Cromer, 1981) time-integration scheme with time step $\Delta \bar{t}$, as described in Thøgersen et al. (2021). At each grid point i and time step, the interface can be either stuck ($\dot{\bar{u}}_i = 0$) or slipping ($\dot{\bar{u}}_i \neq 0$). Static equilibrium in the stuck region, i.e. Eq. (1) with $\ddot{\bar{u}} = 0$, leads in combination with the criterion of Eq. (4) to the following inequality

$$\frac{\bar{u}_{i+1} - 2\bar{u}_i + \bar{u}_{i-1}}{(\Delta \bar{x})^2} - \Gamma \bar{\gamma} \bar{u}_i + \bar{\tau}_{k,i} < 1. \tag{9}$$

Conversely, the dynamics of the sliding portions of the interface is integrated from Eq. (1) as:

$$\ddot{\bar{u}}_i = \frac{\bar{u}_{i+1} - 2\bar{u}_i + \bar{u}_{i-1}}{(\Delta \bar{x})^2} - \Gamma \bar{\gamma} \bar{u}_i + \bar{\tau}_i + \bar{\beta} \frac{\dot{\bar{u}}_{i+1} - 2\dot{\bar{u}}_i + \dot{\bar{u}}_{i-1}}{(\Delta \bar{x})^2}, \tag{10}$$

207 where the scalar $\bar{\beta}$ is a small numerical parameter used to damp spurious high-frequency
208 oscillations and is set to the standard value of $\beta = \sqrt{0.1}\Delta x$ (Knopoff & Ni, 2001; Amund-
209 sen et al., 2012). The set of equations (9)-(10) is closed by the friction law that describes
210 the evolution of $\bar{\tau}_i$ according to Eq. (S.13). More details about the convergence and pa-
211 rameters of the numerical scheme are provided in the Supplementary Information, sec-
212 tion S.2.

213   The initial condition of every simulation corresponds to an interface entirely stuck

214   under a given initial shear stress defined by $\bar{\tau}_k(\bar{x})$. The domain has a finite length $\bar{\mathcal{L}}$ and

215   the boundary conditions on the left and the right edges correspond to $\bar{u}(0) = 0$ and $\bar{u}(\bar{\mathcal{L}}) = $

216   0. In this study, we focus on rupture propagating from the left to the right of the do-

217   main. Rupture nucleation is triggered by defining a region of higher shear stress at the

218   left edges with $\bar{\tau}_k(0) = 1$. Such configuration is depicted in Fig. 1c and describes rup-

219   ture nucleation beyond a barrier (as for instance in Gvirtzman and Fineberg (2021)); how-

220   ever other nucleation processes could be considered with no loss of generality.

221   Figure 3 summarizes the different arrest scenarios and the simulated frictional slip

222   observed after a pulse-like and crack-like rupture. Because $\bar{\tau}_k$ describes the excess of shear

223   pre-stress on top of residual friction, a sharp drop of $\bar{\tau}_k$ toward negative value corresponds

224   to a stress barrier and is presented in Fig. 3B. Frictional weakening during rupture can

225   also involve additional energy dissipation, which in our one-dimensional slip-weakening

226   description corresponds to $\bar{d}_c/2$. A fracture energy barrier can then be simulated by a

227   sharp increase in $\bar{d}_c$ above some critical value $\bar{d}_c^*$, as presented in Fig. 3C. $\bar{d}_c^*$ corresponds

228   to the largest value of $\bar{d}_c$ that can sustain further rupture propagation and is quantita-

229   tively described in the Section 4 below. Finally, frictional ruptures can stop by running

230   out of available energy in the system, which is function of the initial shear stress and whose

231   depletion can be modelled by a progressive decay of $\bar{\tau}_k$, as presented in Fig. 3D.

232   The comparison of rupture styles in Fig. 3 sheds light on the significant difference

233   in terms of final slip that exists between the two frictional rupture modes. Most notably,

234   the profile of slip observed after a pulse-like rupture is much more sensitive to the ar-

235   rest scenarios and keeps a precise record of the local variations of bulk and interface con-

236   ditions compared to the profile of slip observed after crack-like rupture.

4 Theoretical description of the arrest of pulse- and crack-like ruptures

4.1 Equivalence to the Burridge-Knopoff approach

240   The one-dimensional model expressed in its discretized form in Eqs. (9) and (10)

241   is equivalent to Burridge-Knopoff type of models widely used in the literature to describe

242   earthquakes rupture and statistics (e.g., Burridge and Knopoff (1967); Olami et al. (1992);

243   Carlson et al. (1994); Brown et al. (1991); Braun et al. (2009); Trømborg et al. (2014)).

244   Starting from the seminal work of Burridge and Knopoff (1967), the Burridge-Knopoff
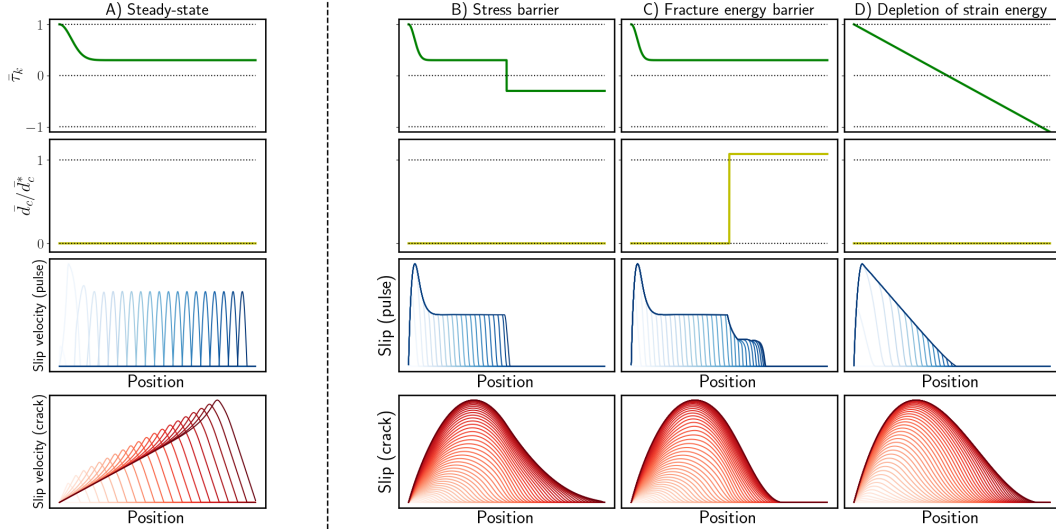
Figure 3. Slip velocities and three arrest scenarios studied in the present study with the resulting final slip profiles observed after a pulse-like (blue) and a crack-like (red) rupture. Slip velocities and slip profiles are calculated by solving numerically the Eq. (1). In each column, the top two panels display the initial profiles of pres-stress and fracture energy along the interface. Rupture is nucleated by a larger value of pre-stress located near $\bar{x} = 0$. A) Steady-state slip velocities for pulse-like and crack-like ruptures. The increasing color shade of each slip profile indicates progression in time. B) A sharp drop of $\bar{\tau}_k$ forms a stress barrier that arrests frictional rupture. C) The frictional rupture is arrested by a sharp increase in $\bar{d}_c$ that corresponds to a fracture energy barrier. D) A linear decay of $\bar{\tau}_k$ progressively reduces the available strain energy to propagate the frictional rupture and eventually arrests it.

245 model for earthquakes consists of a horizontal array of blocks with identical mass con-
246 nected by longitudinal springs. Each block is submitted to a normal force and resists hor-
247 izontal sliding by friction. The system is either loaded by applying a lateral forces or by
248 connecting each block to a moving support via vertical springs, often referred to as leaf
249 springs. Our one-dimensional formulation of Eq. (10) can be obtained from Burridge-
250 Knopoff models by setting blocks mass to unity, lateral springs stiffness to $(\Delta\bar{x})^2$, and
251 the leaf springs stiffness to $\bar{\gamma}$. This analogy is exploited later in the present study to de-
252 rive pulse and crack equations inspired from Burridge-Knopoff models. Our one-dimensional
253 model represents therefore an interesting framework to bridge the discrete description
254 of earthquake dynamics provided in Burridge-Knopoff models to continuum models of

255 faults. The main difference of our approach is that we introduce here a characteristic length

256 scale H, that does not exist in Burridge-Knopoff models.

4.2 One-dimensional energy balance

257

The different contributions to the energy balance of the one-dimensional system correspond to the *elastic energy* $\bar{E}_{\mathrm{el}}$, the *kinetic energy* $\bar{E}_{\mathrm{kin}}$, and the *external work* $\bar{W}_{\mathrm{ext}}$. During the frictional rupture, the work done by the external forces is converted into internal energy such that: $\bar{W}_{\mathrm{ext}} = \bar{E}_{\mathrm{el}} + \bar{E}_{\mathrm{kin}}$. In analogy to Burridge-Knopoff models with $\mathcal{N}$ blocks, the elastic energy corresponds to the potential energy stored in the longitudinal springs and the leaf springs:

$$\bar{E}_{\mathrm{el}} = \sum_{1}^{\mathcal{N}-1} \frac{1}{2}(\Delta\bar{x})^{-2}(\bar{u}_{i+1} - \bar{u}_i)^2 + \Gamma\sum_{1}^{\mathcal{N}} \frac{1}{2}\bar{\gamma}\bar{u}_i^2 \tag{11}$$

or in the continuum form

$$\bar{E}_{\mathrm{el}} = \frac{1}{2}\int_0^{\bar{\mathcal{L}}} \left(\frac{\partial\bar{u}}{\partial\bar{x}}\right)^2 d\bar{x} + \Gamma\frac{1}{2}\int_0^{\bar{\mathcal{L}}} \bar{\gamma}\bar{u}^2 d\bar{x}. \tag{12}$$

Note that the second right-hand-side contribution to the elastic energy in Eq. (12) (i.e. the leaf springs in the Burridge-Knopoff model) only arises for imposed-displacement boundary condition ($\Gamma = 1$, pulses). Similarly, the kinetic energy corresponds to

$$\bar{E}_{\mathrm{kin}} = \frac{1}{2}\int_0^{\bar{\mathcal{L}}} \left(\frac{\partial\bar{u}}{\partial\bar{t}}\right)^2 d\bar{x}. \tag{13}$$

The external work corresponds to

$$\bar{W}_{\mathrm{ext}} = \int_0^{\bar{\mathcal{L}}} \left(\bar{\tau}_k\bar{u} - \bar{W}_b(\bar{u})\right) d\bar{x}. \tag{14}$$

From the definition of $\bar{\tau}_k$ in Eq. (3), the first term on the right-hand side of Eq. (14) combines the work of the external shear stress τ_0 and the work done against residual friction. The second right-hand side term $\bar{W}_b$ accounts for additional dissipation on top of residual friction in case of slip-weakening friction, the so-called *breakdown work*, and is given by

$$\bar{W}_b(\bar{u}) = \int_0^{\bar{u}} \bar{\tau}_f(\mathcal{U})\, \mathrm{d}\mathcal{U}, \tag{15}$$

258 with $\bar{\tau}_f(\bar{u})$ defined in Eq. (S.13).

It is important to note that the initial level of internal energy in the one-dimensional system is set as zero ($\bar{E}_{\mathrm{el}} + \bar{E}_{\mathrm{kin}} = \bar{W}_{\mathrm{ext}} = 0$). Throughout the rupture, the variation of elastic strain energy into a three-dimensional solid of dimensions $\mathcal{L} \times H \times W$ is accounted for in the one-dimensional model by change in $\bar{W}_{\mathrm{ext}}$ and $\bar{E}_{\mathrm{el}}$. For the simplicity of the argument, let us assume Amontons-Coulomb friction and homogeneous slip

along the horizontal extent $\bar{L}$ of a frictional rupture such that only the second right-hand-side term of Eq.(12) contributes to the elastic energy. The amount of energy released by the rupture into the system corresponds to

$$\bar{E}_r = \bar{W}_{\text{ext}} - \bar{E}_{\text{el}} = \bar{L}\left(\bar{\tau}_k \bar{u} - \frac{1}{2}\Gamma\bar{\gamma}\bar{u}^2\right), \tag{16}$$

which is converted into kinetic energy. Frictional rupture is *energetically admissible* if $\bar{E}_r \geq 0$.

For imposed-stress boundary conditions ($\Gamma = 0$), frictional slip is admissible as long as $\bar{\tau}_k \geq 0$, and the larger the slip the more energy is released in the system. Conversely, for imposed-displacement boundary conditions ($\Gamma = 1$), part of the work injected by the pre-stress in the system goes into the leaf spring elastic energy, such that frictional slip is only admissible for $0 \leq \bar{u} \leq 2\bar{\tau}_k/\bar{\gamma}$, with the upper bound being equivalent to the steady-state slip solution of Eq. (7). This different energy transfer between stress- and displacement-controlled conditions explains why, in the wake of the propagating rupture, the interface re-stick (i.e pulse-like rupture) for $\Gamma = 1$ whereas sliding continues in the form of a crack-like rupture for $\Gamma = 0$. Physically, this one-dimensional energy balance describes the fact that the shear stress τ_0 remains constant in the three-dimensional solid during the rupture for imposed-stress boundary conditions, whereas τ_0 progressively drops with frictional slip if the displacement is imposed at the top surface of the block, according to Figure 2. In the Supplementary Information sections S.3 and S.4, this one-dimensional energy balance is exploited further to describe frictional rupture beyond the homogeneous steady-state simplification in order to propose pulse and crack arrest equations which are summarized hereafter.

4.3 Pulse arrest equations

First, we follow the approach proposed by Elbanna and Heaton (2012) and derive a pulse equation by integrating the energy balance between the nucleation site $\bar{x} = 0$ to the leading tip of the pulse $\bar{x} = \bar{L}$. Next, we assume that the ruptured area is larger than the width of the pulse $\bar{L} \gg \bar{\omega}$ to neglect the contribution of the regions within the pulse width and obtain the following ordinary differential equation:

$$\frac{\partial^2 \bar{u}_p}{\partial \bar{x}^2} = \bar{\gamma}\bar{u}_p - 2\bar{\tau}_k + \frac{2\bar{W}_b(\bar{u}_p)}{\bar{u}_p}, \tag{17}$$

with $\bar{u}_p$ being the final slip reached in the wake of the traveling pulse. The detailed derivation of Eq. (17) can be found in the section S.3.
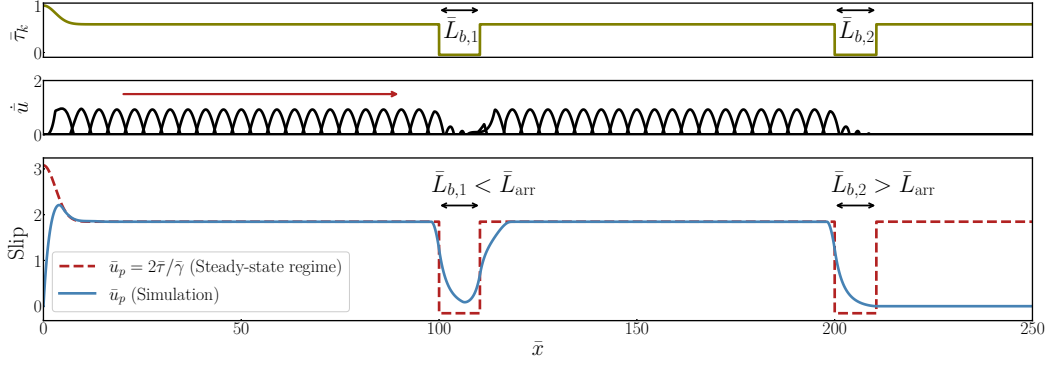
Figure 4. Example of slip pulse simulation. *Top*: Profile of the initial pre-stress, $\bar{\tau}_k$, with a Gaussian stress concentration introduced on the left side of the domain to nucleate frictional rupture. Stress barriers with similar amplitude $\bar{\tau}_{k,b} = -10^{-4}$ but various lengths $\bar{L}_{b,i}$ are placed along the fault at $\bar{x} = 100$ and $\bar{x} = 200$. *Middle*: Snapshots of slip velocity at different time steps, showing slip pulse propagation in the direction of the red arrow. Note that the pulse crossed the first barrier, but was stopped by the longer second barrier. *Bottom*: Final slip profile compared to the steady-state regime. A propagating pulse can cross a barrier of length smaller than the arrest length $\bar{L}_{\mathrm{arr}}$ but is arrested by a barrier that is larger than $\bar{L}_{\mathrm{arr}}$

.

4.3.1 Stress barriers

This arrest scenario is studied by simulating a steadily propagating pulse under a given initial stress $\bar{\tau}_{k,0}$ that reaches a region of lower pre-stress at $\bar{x} = \bar{x}_b$, as shown in Fig. 4. If the shear stress within the barrier $\bar{\tau}_{k,b}$ is still positive, a steady-state pulse solution exists and the final slip evolves toward the new steady-state according to Eq. (7). If $\bar{\tau}_{k,b}$ is negative (as in Fig 4), sustained pulse propagation is no longer possible such that the rupture will be arrested for barriers that exceed a critical length defined as $\bar{L}_{\mathrm{arr}}$. The pulse equation (17) can be used to predict the decay of slip observed in Fig. 4 within a barrier of negative pre-stress. For negligible breakdown work (i.e. Amontons-Coulomb friction with $\bar{W}_b = 0$), the general solution of Eq. (17) is the sum of two exponential functions. As shown in Figure S2, the pulse arrest equation Eq. (17) can be used to derive different predictions of the decay of frictional slip within the barrier from its initial steady-state value $u_p = 2\bar{\tau}_k/\bar{\gamma}$. For instance, the following solution is obtained by searching for solution where both $\bar{u}_p(\bar{x}')$ and its first derivative are equal to zero at the arrest

location:

$$\bar{u}_p(\bar{x}') = \frac{-2\bar{\tau}_{k,b}}{\bar{\gamma}}\Big(\cosh\big((\bar{x}' - \bar{L}_{\text{arr}})\sqrt{\bar{\gamma}}\big) - 1\Big), \tag{18}$$

with $\bar{x}' = \bar{x} - \bar{x}_b$, where x_b is the position at which the barrier starts. Remembering that $\bar{\tau}_{k,b} < 0$, the equation above has a positive root $\bar{u}_p(\bar{x}' = \bar{L}_{\text{arr}}) = 0$ which can be used to predict the arrest length:

$$\bar{L}_{\text{arr}} = \bar{\gamma}^{-\frac{1}{2}}\text{arccosh}\Big(\frac{\bar{\tau}_{k,0} - \bar{\tau}_{k,b}}{-\bar{\tau}_{k,b}}\Big). \tag{19}$$

281   Figure 5(A) compares this theoretical prediction with the numerical simulations for var-

282   ious stress barriers $(-\bar{\tau}_{k,b})$ with different initial prestress $(\bar{\tau}_{k,0})$ and moduli $\bar{\gamma}$. The the-

283   oretical prediction of Eq. (19) captures well the trend observed in the simulations but

284   systematically underestimates the simulated arrest length. This underestimation comes

285   from the simplification behind the pulse arrest equation (17), which neglects the finite

286   width of the pulse and associated mechanical energy. As shown in Figure S2, frictional

287   slip in the simulations starts decaying before the barrier location due to the finite width

288   of the pulse.

289   ### 4.3.2 Fracture energy barriers

If the contribution of the breakdown energy is non-negligible (slip-weakening friction), two end-member situations can occur. In a first case, frictional weakening is complete in the wake of the rupture, such that the breakdown work is constant and equates the fracture energy prescribed in the slip weakening friction law, $\bar{W}_b = \bar{G}_c = \bar{d}_c/2$. Equation (17) is a non-linear ordinary differential equation, but the possibility for smoothly travelling pulse can nevertheless be investigated by neglecting the second-order derivative, which leads to the following slip solution behind the travelling pulse:

$$\bar{u}_p = \frac{\bar{\tau}_k}{\bar{\gamma}}\Big(1 + \sqrt{1 - \frac{\bar{d}_c\bar{\gamma}}{\bar{\tau}_k^2}}\Big). \tag{20}$$

Note how Eq. (20) leads to the steady-state solution for Amontons-Coulomb friction of Eq. (7) as $\bar{d}_c \to 0$. Interestingly, neglecting the contribution of the fracture energy in the steady-state pulse solution leads to an overestimation of the final slip by at most a factor two. The solution Eq. (20) leads to the definition of a critical value of $\bar{d}_c$, above which sustained pulse propagation is no longer admissible:

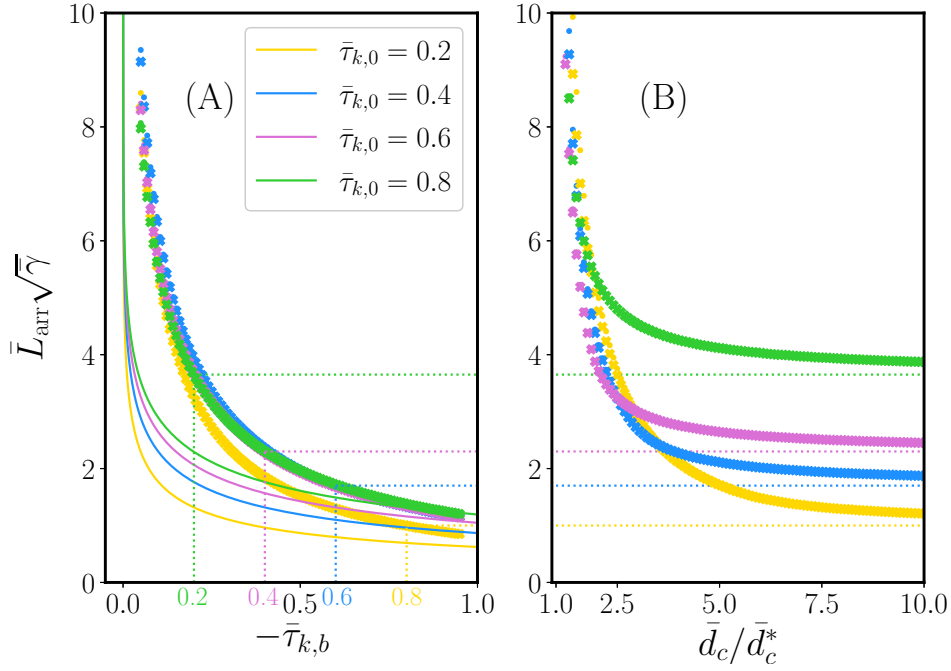$$\bar{d}_c^* = \bar{\tau}_k^2/\bar{\gamma}. \tag{21}$$

Figure 5. Arrest length for slip pulse in presence of stress (A) and fracture energy (B) barriers. The solid lines on the plot (A) correspond to the theoretical prediction given by Eq. (19). Color symbols correspond to simulation results at different initial stresses $\tau_{k,0}$ for $\bar{\gamma} = 0.65$ (circle) and $\bar{\gamma} = 2.0$ (cross). The dashed horizontal lines highlight how the stress barrier with amplitude $\bar{\tau}_{k,b} = \tau_{k,0} - 1$ gives the asymptotic value of the arrest length for tough fracture energy barriers $\bar{d}_c \gg \bar{d}_c^*$.

Using Eqs. (20), one can rewrite the pulse equation (17) and defined ð as

$$\frac{\partial^2 \bar{u}_p}{\partial \bar{x}^2} = \bar{\gamma} \bar{u}_p - 2\bar{\tau}_k + \frac{\bar{d}_c}{\bar{u}_p} = \bar{\gamma} \bar{u}_p - \bar{\tau}_k \left(2 - \frac{\bar{d}_c/\bar{d}_c^*}{1 + \sqrt{1 - \bar{d}_c/\bar{d}_c^*}} \right) \equiv \bar{\gamma} \bar{u}_p - ð \bar{\tau}_k, \qquad (22)$$

with $1 \leq ð \leq 2$ being a constant that depends on the interface fracture energy. For the largest admissible fracture energy ($\bar{d}_c = \bar{d}_c^*$), one has $ð = 1$, whereas for zero fracture energy $ð = 2$.

As in the case of stress barriers, a fracture energy barrier with $\bar{d}_c > \bar{d}_c^*$ will arrest the rupture if its length is larger than some arrest length $\bar{L}_{\mathrm{arr}}$. This leads to the other situation for which frictional weakening is incomplete in the wake of the rupture ($\bar{W}_b < \bar{d}_c/2$). The integration of the breakdown work according to Eq. (15) leads to the follow-

ing ordinary differential equation:

$$\frac{\partial^2 \bar{u}_p}{\partial \bar{x}^2} = \left(\bar{\gamma} - \frac{1}{\bar{d}_c}\right)\bar{u}_p - 2(\bar{\tau}_k - 1). \tag{23}$$

For very large $\bar{d}_c$, the equation above is identical to the one describing a stress barrier with $\bar{\tau}_{k,b} = \bar{\tau}_k - 1$. Physically, this means that there is not enough slip and energy to drive the weakening of the interface within the barrier such that frictional stress stays close to the static value (corresponding to $\bar{\tau} = \bar{\tau}_k - 1$) throughout the width of the pulse. An important implication is that any fracture energy barrier with a length shorter than

$$\bar{L}^*_{\mathrm{arr}} = \bar{L}_{\mathrm{arr}}(\bar{\tau}_{k,b} = \bar{\tau}_{k,0} - 1) \tag{24}$$

cannot stop a propagating slip pulse regardless of its fracture energy amplitude. The figure 5(B) presents the two asymptotic situations that describe the arrest of pulse-like rupture by a fracture energy barrier: $\bar{L}_{\mathrm{arr}}$ diverges as $d_c \to \bar{d}_c^*$, whereas for $d_c \to \infty$ the arrest length converges towards $\bar{L}^*_{\mathrm{arr}}$.

4.3.3 Progressive decay of available strain energy

Ruptures can also be arrested by smoothly decaying prestress, $\bar{\tau}_k$. Indeed, earthquakes typically nucleate in a critically stressed portion of a fault before reaching subcritically stressed regions. In the one-dimensional model, stress criticality is described by the dimensionless variables $\bar{\tau}_k$ (with critical values corresponding to $\bar{\tau}_k > 1$). Pulse rupture in a smoothly decaying pre-stress can be described using the pulse arrest equation. For example with a linearized decaying profile of the form $\bar{\tau}_k(\bar{x}) = 1 - \bar{\alpha}\bar{x}$, the following final slip profile satisfies Eq. (17):

$$\bar{u}_p = \frac{2}{\bar{\gamma}}\left(1 - \bar{\alpha}\bar{x} - \exp(-\bar{x}\sqrt{\bar{\gamma}})\right). \tag{25}$$

Similarly, for a quadratic decay of the prestress profile of the form $\bar{\tau}_k = 1 - \bar{\lambda}\bar{x}^2$, the following profile of slip can be predicted using the pulse equation:

$$\bar{u}_p = \frac{2}{\bar{\gamma}}\left((1 - 2\bar{\lambda}\bar{\gamma}^{-1})(1 - \exp(-\bar{x}\sqrt{\bar{\gamma}})) - \bar{\lambda}\bar{x}^2\right). \tag{26}$$

Figure 6 validates the theoretical predictions (25) and (26) derived from the pulse equation with numerical simulations. Accounting for the contribution of the growing exponential term $\sim \exp(\bar{x}\sqrt{\bar{\gamma}})$, which was neglected in the derivation of Eqs. (25) and (26), could further improve the predicted slip closed to the arrest position.

302   For slowly decaying prestress (i.e., $\bar{\alpha}; \bar{\lambda} \ll 1$), both equations (25) and (26) pre-

303   dict that the rupture arrests at the location where $\bar{\tau}_k = 0$, which leads to $L_{\mathrm{ar}} \cong \bar{\alpha}^{-1}$

304   and $L_{\mathrm{ar}} \cong \bar{\lambda}^{-1/2}$, respectively for the linear and quadratic prestress. In dimensional units,

305   the rupture is then expected to arrest where the initial shear stress τ_0 becomes smaller

306   than residual friction $\mu_k \sigma_n$.

307   Remarkably, these generic decaying loading conditions produce asymmetric, tri-

308   angular, slip profiles reminiscent of the slip profiles reported in natural fault zones (Manighetti

309   et al., 2005, 2009). After nucleation, the rapid slip rise is governed by elasticity and the

310   exponential term $(1-\exp(-\bar{x}\sqrt{\bar{\gamma}}))$. Post peak, the slow decay mimics the profile of ini-

311   tial stress and is governed by the linear term of Eq. (25) or the quadratic decay in Eq
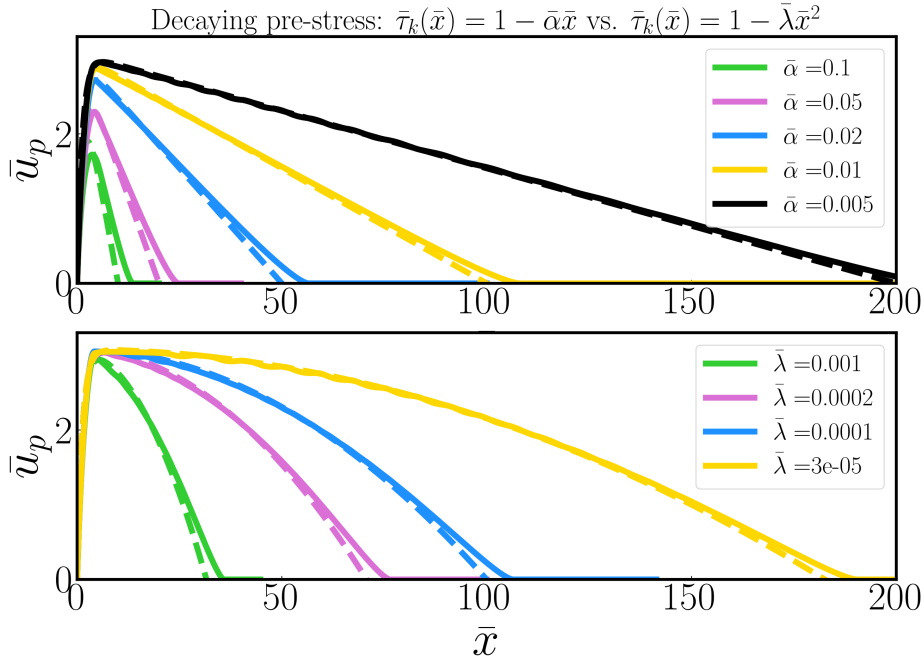
312   (26).

Figure 6.   Profile of final slip caused by a pulse-like rupture propagating towards a region
with decaying pre-stress: simulations (solid lines) versus the analytical predictions (dashed-lines)
derived from the pulse arrest equation (17). Top: Linearly decaying pre-stress with final slip
predicted by Eq. (25). Bottom: Quadratically decaying pre-stress with final slip predicted by Eq.
(26)

313 ### 4.4 Crack arrest equations

Crack-like rupture in Burridge-Knopoff models have received more attention in the literature compared to pulses. Past works (e.g. Trømborg et al. (2011); Amundsen et al. (2012)) showed that the arrest of cracks in these models can be well predicted using the net shear force acting on the sliding block just ahead of the propagating tip, which corresponds, in our one-dimensional model, to the following integral:

$$\bar{K}(\bar{L}) = \int_0^{\bar{L}} \bar{\tau}_k(\bar{x}) \, \mathrm{d}\bar{x}. \tag{27}$$

314 Crack-like ruptures have different energy budget than pulses. First, kinetic energy dur-
315 ing the rupture is not concentrated near the propagating tip but spreads over the en-
316 tire ruptured area. Second, there is no contribution from the leaf spring elastic energy
317 because $\Gamma = 0$ in Eq. (12). Therefore, the work done by the external stress W_{ext} is con-
318 verted into strain and kinetic energy within the crack and corresponds to the energy re-
319 leased by the rupture.

To illustrate the difference of energy budget governing pulse and crack dynamics, we derive the steady-state solution for a propagating crack under homogeneous conditions in the section S.4.1 of the Supplementary Information. Using this steady-state solution, we can compute the energy released by the rupture, which corresponds to

$$\bar{E}_{\text{crack}} = \frac{\bar{\tau}_k^2 \bar{L}^3}{6\bar{v}_c(\bar{v}_c + 1)} \tag{28}$$

for a crack of size $\bar{L}$ propagating at speed $\bar{v}_c$. For homogeneous conditions, $K(\bar{L}) = \bar{\tau}_k \bar{L}$ can then be related to $\bar{E}_{\text{crack}}$ by expressing the rate of energy release per unit crack advance, $\bar{G}$:

$$\bar{G}(\bar{L}, \bar{v}_c) = \frac{\mathrm{d}\bar{E}_{\text{crack}}}{\mathrm{d}\bar{L}} = \frac{\bar{\tau}_k^2 \bar{L}^2}{2\bar{v}_c(\bar{v}_c + 1)} = \bar{K}^2 \bar{\mathcal{A}}(\bar{v}_c). \tag{29}$$

320 By analogy with dynamic fracture mechanics (e.g. Freund (1998)), $\bar{K}$ and $\bar{G}$ correspond
321 to the one-dimensional stress intensity factor and the energy release rate, whereas $\bar{\mathcal{A}}$ is
322 some universal function of the rupture speed.

323 ### 4.4.1 Stress barriers

For a stress barrier, the arrest location of crack-like rupture is well predicted by the first position along the crack path where the net force acting on the sliding element ahead of the tip becomes zero (Trømborg et al., 2011; Amundsen et al., 2012). Using Eq. (27), the predicted arrest length $\bar{L}_{\text{arr}}$ of crack-like rupture in the one-dimensional model

can be readily defined as $\bar{K}(\bar{x}_b + \bar{L}_{\mathrm{arr}}) = 0$, which implies that

$$\bar{L}_{\mathrm{arr}} = -\frac{\bar{x}_b \bar{\tau}_{k,0}}{\bar{\tau}_{k,b}}, \tag{30}$$

recalling that $\bar{\tau}_{k,b}$ has to be negative to form a stress barrier. Unlike pulse-like rupture (see Eq. (19)), the arrest length of crack also depends on the position of the barrier $\bar{x}_b$. This is explained by the fact that the energy released by a crack depends on its size $\bar{L}$ to a cubic power (see Eq. (28)), whereas the energy released by a steadily propagating pulse is constant and only depends on $\bar{\tau}_k$ (see Eq. S.30 and Supplementary Information section S.3.4 for more details).

4.4.2 Fracture energy barriers

As discussed in the context of pulses, the two characteristic quantities $\bar{d}_c^*$ and $\bar{L}_{\mathrm{arr}}^*$ can be similarly defined for cracks. $\bar{d}_c^*$ corresponds to the minimal amount of fracture energy required to arrest the rupture (sustained rupture growth is admissible for $\bar{d}_c < \bar{d}_c^*$). $\bar{L}_{\mathrm{arr}}^*$ corresponds to the minimum barrier length required to arrest the rupture (no fracture energy barrier with size $\bar{L}_{\mathrm{arr}} < \bar{L}_{\mathrm{arr}}^*$ can arrest a propagating rupture). The main difference is that for crack-like rupture both $\bar{d}_c^*$ and $\bar{L}_{\mathrm{arr}}^*$ depend on the size of the crack ($\bar{L} = \bar{x}_b$).

As in the case of pulse-like rupture, $\bar{L}_{\mathrm{arr}}^*$ corresponds to the arrest length caused by a stress barriers with $\bar{\tau}_{k,b} = \bar{\tau}_k - 1$, which leads to the following expression using (30)

$$\bar{L}_{\mathrm{arr}}^*\left(\bar{\tau}_k, \bar{x}_b\right) = \frac{\bar{x}_b \bar{\tau}_k}{1 - \bar{\tau}_k}. \tag{31}$$

As discussed for pulse-like rupture, $\bar{L}_{\mathrm{arr}}^*$ above governs rupture arrest in the asymptotic limit $\bar{d}_c \to \infty$, for which frictional weakening is limited and $\bar{\tau}_f$ stays near the static value.

The other end-member situation corresponds to fully developed frictional weakening such that $\bar{W}_b = \bar{G}_c = \bar{d}_c/2$. The one-dimensional dynamic fracture energy balance ($\bar{G} = \bar{G}_c$) can be used together with Eq. (29) to define critical fracture energy following the derivation detailed in the Supplementary Information, section S.4:

$$\bar{d}_c^*(\bar{\tau}_k, \bar{x}_b) = \left(\frac{4\bar{x}_b}{3}\right)^2 (1 - \bar{\tau}_k^2)\left(1 - \sqrt{1 - \bar{\tau}_k^2}\right). \tag{32}$$

Figure 7 tests the predictions of $\bar{L}_{\mathrm{arr}}^*$ (31) and $\bar{d}_c^*$ (32) against simulations that span several orders of magnitude of fracture energy barrier and arrest length. First, it shows that the simplifications behind Eq. (32) gives an accurate prediction for moderate pre-stress.

At large pre-stress, dynamical effects associated to fast crack speed tend to overshoot the prediction of $\bar{L}_{\text{arr}}$ in Eq. (S.44) and, thereby, $\bar{d}_c^*$. Second, the arrest of crack-like rupture is much sharper than in the case of slip pulse, such that $\bar{L}_{\text{arr}}^*(\bar{x}_b)$ (31) always provides a good approximation of the arrest length by a fracture energy barrier.
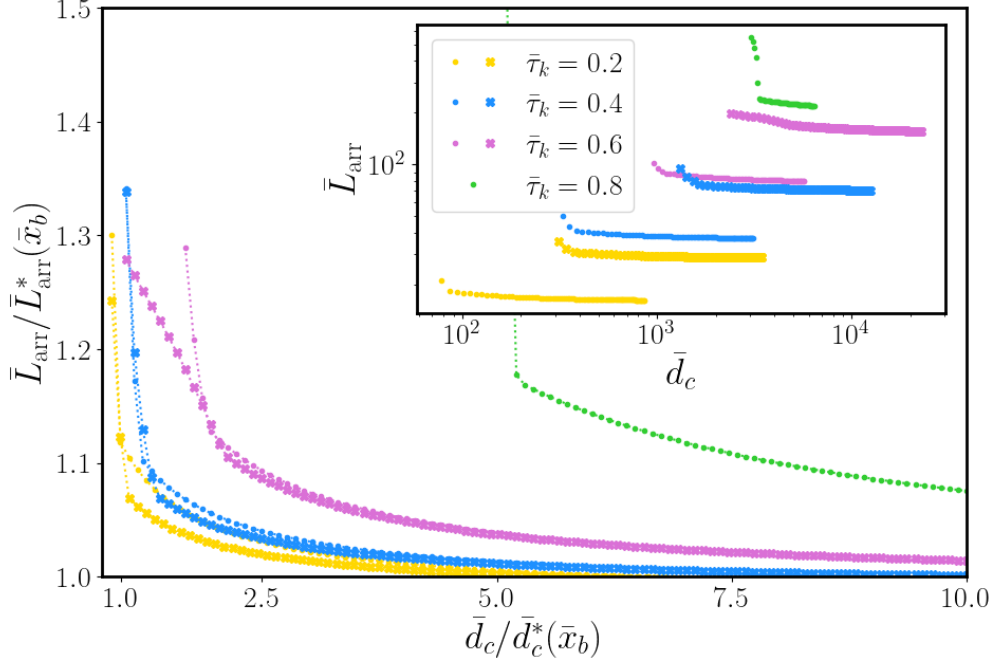

Figure 7. Arrest length of crack-like rupture stopped by a fracture energy barrier simulated for different values of initial stress $\bar{\tau}_k$ and fracture energy amplitude $\bar{d}_c$. The markers identify simulations with barrier size $\bar{x}_b = 50$ (dots) and $\bar{x}_b = 100$ (crosses). The inset shows the raw data that spans several orders of magnitude in $\bar{L}_{\text{arr}}$ and $\bar{d}_c$, and that are collapsed in the main plot using the definitions of $\bar{d}_c^*$ in Eq. (32) and $\bar{L}_{\text{arr}}^*$ in Eq. (31).

4.4.3 Progressive decay of available energy

As in the case of stress barriers, the one-dimensional stress intensity factor defined in Eq. (27) can be readily used to predict the arrest of a crack-like rupture under smoothly decaying pre-stress conditions as $\bar{K}(\bar{L}_{\text{arr}}) = 0$. In the case of the linearly decaying shear stress $\bar{\tau}_k = 1 - \bar{\alpha}\bar{x}$, the arrest length corresponds then to $\bar{L}_{\text{arr}} = 2/\bar{\alpha}$ and is twice larger than in the case of a pulse-like rupture. For quadratic decay of the pre-stress $\bar{\tau}_k = 1 - \bar{\lambda}\bar{x}^2$, the arrest length corresponds then to $\bar{L}_{\text{arr}} = \sqrt{3/\bar{\lambda}}$. Using this arrest prediction,

354 the one-dimensional energy balance can be used to derive a theoretical prediction of the

355 profile of the final slip $\bar{u}_p$, as detailed in the Supplementary Information, section S.4.2.

356 As shown in Figure 8, the solution allows to collapse the final slip profile simulated with

357 different values of $\bar{\alpha}$ and $\bar{\lambda}$. Important differences exist between the slip profile after pulse-

358 like rupture shown in Fig. 6 and the slip observed after crack-like rupture in Fig. 8. Slip

359 profiles after pulse-like rupture record the initial variations of the prestress before the

360 rupture, whereas crack-like rupture tends to homogenize and average local variations of

361 prestress. Mechanically, this difference arises because crack releases energy over the en-

362 tire rupture length $\bar{L}$, whereas pulse energy balance is more local and concentrated in

363 the thin width $\bar{\omega}$ near the rupture tip. Mathematically, this difference translates into slip

364 profile governed by a differential equation for pulses, Eq. (17), versus an integral equa-

365 tion that governs $\bar{u}_p$ for cracks, Eqs. (S.46)-(S.47). Consequently, when propagating to-

366 wards decaying pre-stress, slip pulses produce asymmetric slip profiles, whereas crack-

367 like ruptures produce slip profiles where the relative position of the maximum slip of-

368 ten lies between one third and one half of the arrest distance $\bar{L}_{\text{arr}}$. Consequently, in this

369 setup, pronounced asymmetric, triangular, slip profiles are exclusively the signature of

370 pulse-like ruptures.

5 Discussion

5.1 Connection to existing earthquake models

373 The differential equation solved in our one-dimensional model can be related to the

374 equation of motion of spring-block systems used in Burridge-Knopoff models (Burridge

375 & Knopoff, 1967; Burridge & Halliday, 1971). This analogy is directly used in the present

376 study to calculate the energy balance and we propose analytical predictions of the rup-

377 ture dynamics. Our one-dimensional system of equations brings an additional length scale

378 H that is missing in the classical spring-block models and allows to bridge them to the

379 continuum elastic description of faulting. Indeed, the one-dimensional model allows for

380 capturing several characteristics of rupture dynamics described in two- and three-dimensional

381 models of fault under different boundary conditions.

382 Under imposed-stress boundary conditions ($\Gamma = 0$), ruptures simulated with the

383 one-dimensional model have similar dynamics to that of cracks propagating in unbounded

384 elastic domain. In such setup, the most frequent rupture mode corresponds to the prop-

385 agation of a shear crack (e.g. Kostrov, 1966; Ida, 1972), whereas slip-pulses are inher-
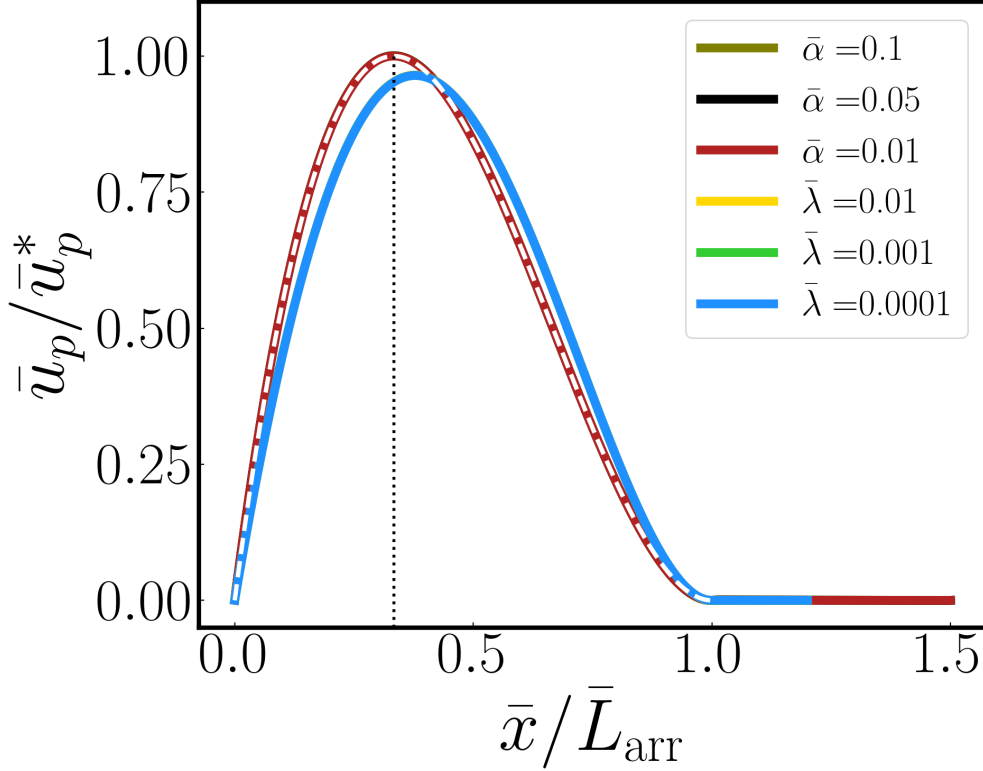
Figure 8. Simulation (solid line) versus theoretical prediction (white dashed-line) of the final slip profile observed for a crack-like rupture with a linear decay ($\bar{\tau}_k(\bar{x}) = 1 - \bar{\alpha}\bar{x}$) or a quadratic decay ($\bar{\tau}_k(\bar{x}) = 1 - \bar{\lambda}\bar{x}^2$) of the pre-stress. As derived in Supplemental Information, section S.4.2, $\bar{L}_{\mathrm{arr}}$ corresponds respectively to $\bar{\alpha}/2$ and $\sqrt{3/\bar{\lambda}}$ for the linear and quadratic decays, whereas the maximum slip $\bar{u}_p^*$ is respectively given by $4/(27\bar{\alpha}^2)$ and $2/(9\bar{\lambda})$. The position of maximum slip is most often located near $\bar{x} = \bar{L}_{\mathrm{arr}}/3$, as highlighted by the vertical black dotted line.

386 ently unstable and emerge under specific loading and interface conditions (Zheng & Rice,

387 1998; Gabriel et al., 2012; Brener et al., 2018; Brantut et al., 2019). As in the one-dimensional

388 model under imposed-stress boundary conditions, the system supplies an unlimited amount

389 of energy to the propagating rupture and promotes crack-like rupture whose energy re-

390 lease rate increases with the rupture size. The one-dimensional setup includes an addi-

391 tional length scale H, such that the crack energy release rate scales as $G \sim (\Delta\tau)^2 \mathcal{G}^{-1} L^2 H^{-1}$

392 instead of the scaling $G \sim (\Delta\tau)^2 \mathcal{G}^{-1} L$ relevant for circular cracks in an infinite domain.

393 Apart from this different scaling, the crack arrest criterion predicted by Eq. (27) is the

394 one-dimensional analogue of the shear fracture criterion that was successfully used to

395   predict the arrest of frictional rupture in laboratory experiments (Kammer et al., 2015;

396   Bayart et al., 2016; Ke et al., 2018).

397   Under displacement-controlled boundary conditions ($\Gamma = 1$), the rupture dynam-

398   ics is substantially different and pulse-like rupture becomes the prominent failure mode.

399   This fundamental change is caused by the finite amount of strain energy available for

400   rupture under imposed-displacement boundary conditions. Such transition is analogous

401   to the change in the rupture dynamics reported in three-dimensional simulations of earth-

402   quake ruptures with large aspect ratio $L \gg W$ (Day, 1982; Weng & Ampuero, 2019)

403   or if the fault is surrounded by a damaged region with high elastic contrast (Idini & Am-

404   puero, 2020). As depicted in Fig. 1, the relevant type of boundary conditions applied

405   at a distance H from the fault corresponds to imposed-displacement. For subduction zones

406   (Fig. 1a), the plate is loaded by and coupled to the downward motion of the viscous up-

407   per mantle. Due to the no-slip boundary conditions between the elastic plate and the

408   viscous upper mantle, a constant displacement at the plate edge is a reasonable approx-

409   imation over the duration of the dynamic ruptures. For the strike-slip system (Fig. 1b),

410   slip along the fault leads to an associated stress drop in the compliant elastic fault core

411   of thickness H. The continuity of displacements and stress at the boundary between the

412   compliant fault core and the stiffer wall-rock implies that the associated displacement

413   at this boundary will be much smaller than interfacial slip. Therefore, imposed-displacement

414   boundary conditions is also relevant in such configurations. (see section C2 of Thøgersen

415   et al. (2021) for more details).

416   Recently, Weng and Ampuero (2019) showed how the Linear Elastic Fracture Me-

417   chanics solution for a thin-strip geometry (Marder, 1998) can accurately describe earth-

418   quake dynamics at high aspect ratio L/W. Using the thin-strip solution, they proposed

419   a *fault rupture potential* than can be used to predict the arrest and the size of earthquakes.

420   As detailed in Section S.5, their thin-strip solution and associated fault rupture poten-

421   tial are complementary to the approach proposed in the present study, which brings es-

422   timates of the final slip profile and associated stress drop and generalizes the descrip-

423   tion beyond the Linear Elastic Fracture Mechanics assumption (finite fracture energy,

424   small scale-yielding conditions, smooth rupture acceleration). Remarkably, the two de-

425   scriptions share the same fracture energy criterion to predict rupture deceleration, i.e.

426   $\bar{d}_c/\bar{d}_c^* = G_c/G_0 > 1$ and lead to similar arrest length prediction in the limit $\bar{d}_c \rightarrow \bar{d}_c^*$

427   (see Fig. S4).

428   **5.2 Natural controls on rupture arrest**

429   Previous studies have proposed that earthquake rupture may be arrested by the
430 following situations:

431   • Low amount of available elastic strain energy, where the rupture enters a region
432   that precludes a stress drop (Husseini et al., 1975). This mechanism is related to
433   a stress heterogeneity barrier, where an uneven stress distribution, e.g. as induced
434   by the history of past earthquakes, stops the earthquake (Aki, 1979).
435   • Barriers along the trajectory of the rupture, such as increase in fracture energy
436   or geometrical heterogeneities may arrest a rupture. Such situations can arise when
437   the rupture enters a region of intact rock at a fault tip (Husseini et al., 1975)) or
438   along fault geometrical barriers such as bends, steps and jogs (Aki, 1979; Harris
439   et al., 2002; Magistrale & Day, 1999).

Our minimal model is able to represent these arrest scenarios with only two control parameters in case of Amontons Coulomb friction ($\bar{\tau}_k$ and $\bar{\gamma}$), and with three parameters ($\bar{\tau}_k, \bar{d}_c$, and $\bar{\gamma}$) in case of slip-weakening friction. The most important parameters are the pre-stress, $\bar{\tau}_k$, and the fracture energy, $\bar{d}_c$. As discussed in the previous section, the one-dimensional slip pulse solution associated with imposed-displacement boundary conditions ($\Gamma = 1$) provides an accurate description of large planar earthquake rupture depicted in Fig. 1. In this context, we propose a pulse equation, summarized hereafter, that describes the propagation and arrest of frictional rupture:

$$\frac{\partial^2 \bar{u}_p}{\partial \bar{x}^2} = \bar{\gamma}\bar{u}_p - \eth\bar{\tau}_k. \tag{33}$$

440   We recall that $\bar{\tau}_k$ describes the pre-stress along the fault before the rupture, $\bar{u}_p$ corre-
441 sponds to the total slip observed along the fault after the rupture, and $\eth$ is a parame-
442 ters defined in Eq. (22) and whose value lies between 1 (for the largest admissible frac-
443 ture energy) and 2 (for negligible fracture energy). We next discuss how to connect the
444 natural arrest scenarios presented above, to the different scenarios of uneven distribu-
445 tions of pre-stress and fracture energy analysed for our minimal model.

446   *5.2.1 Geometrical barriers – fault bends*

447   Fault bends are observed to stop or slow ruptures (e.g. (Elliott et al., 2015; King
448 & Nábělek, 1985)). One can parameterize this geometrical structure by a change in pre-

(a) Fault geometry barrier   (b) Breakdown energy barrier   (c) Stress decay barrier
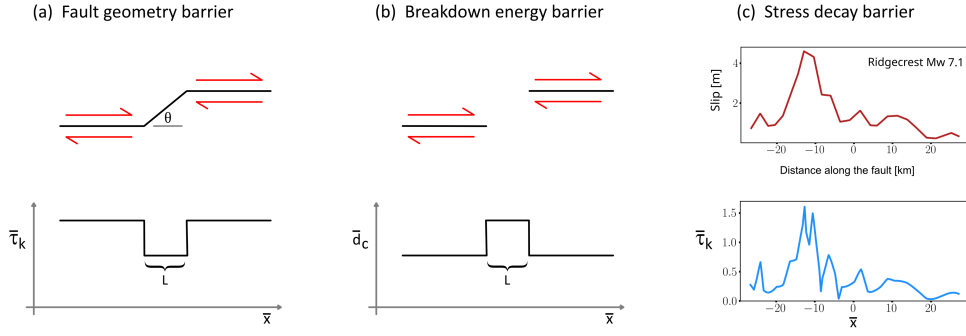
Figure 9. Cartoon of arrest scenarios and how they correspond to the different arrest scenarios discussed in Figure 3. a) A fault bend with an angle θ and length L corresponds to a decrease in $\bar{\tau}_k$. b) A fault step with offset of length L corresponds to a fracture energy barrier, and is represented by a lateral increase of $\bar{d}_c$ in our model. c) Top plot shows the profile of slip from the $M_w 7.1$ 2019 Ridgecrest earthquake published by Chen et al. (2020). The bottom plot shows the corresponding profile of dimensionless prestress computed using our pulse equation (33). See more details in section S.6.

449   stress (e.g. (Lozos et al., 2011)). For example, Fig. 9a illustrates a restraining bend. Af-
450   ter projection of remotely applied principle stresses on inclined planes, it is readily shown
451   that the shear stress, τ_0, on the bend segment is reduced relative to the straight fault
452   segments, while the normal stress σ_n on the bend is increased relative to the straight fault
453   segment, which we assume is favorably oriented for sliding. Both these trends act to re-
454   duce the ratio $\bar{\tau}_0/\sigma_n$ in Eq. (3) on the bend. Therefore, a restraining bend (Fig. 9a) is
455   a similar scenario to the stress barrier displayed in Fig. 4B. Since scaling in Eq. (3) as-
456   sumed a constant σ_n, we note that the calculation of $\bar{\tau}_k$ must be modified to account for
457   spatially varying $\sigma_n(x)$ and to quantify the reduction of pre-stress over the bend segment.
458   As sketched in Fig. 9a, the amplitude of the pre-stress within the barrier depends
459   on the angle of the restraining bend θ and its length depends on the bend segment length.
460   One can therefore use our minimal model to predict quantitatively at which angles and
461   which lengths of bend segments the rupture will stop. Our pulse arrest relationship of
462   Eq. (19), and the corresponding Figure 5A, predict that the steeper the bend angle, the
463   shorter the arrest length will be because $\bar{\tau}_{k,b}$ will decrease with increasing bend angle.

464   Thus, we can qualitatively predict that pulses will traverse relatively long shallowly in-

465   clined bends, but will be stopped by much shorter steep bends, in agreement with the

466   figure 4b in Lozos et al. (2011).

467   For cracks, Eq. (30) predicts a different arrest scenario than for pulses. While pulse

468   arrest is independent of where a fault bend is located relative to the hypocenter, under

469   constant stress boundary conditions cracks should be able to traverse longer and steeper

470   bends the further they are from the hypocenter, since they release more and more en-

471   ergy.

5.2.2   *Geometrical barrier – step-overs and offsets*

473   It is known that earthquakes often stop at fault step-overs or offsets, a situation

474   depicted in Fig. 9b, upper panel. Barka and Kadinsky-Cade (1988) suggested that fault

475   step-overs and offsets exceeding five kilometers and angles exceeding 30° mostly stop earth-

476   quakes. Here, we follow Husseini et al. (1975) and suggest that the region of the step-

477   over, which contains unbroken rock, can be described as a region with larger fracture en-

478   ergy, as in Fig. 9b. We showed in Fig. 5B that for pulses the arrest length $\bar{L}_{arr}$ increases

479   as the material in the step-over between segments becomes weaker, i.e. $\bar{d}_c$ decreases. The

480   value of $\bar{L}_{arr}$ is shown to range between $\sim 1-10$. If we bring this back to dimensional

481   terms, the arrest length is in the range $H-10H$. In the scenario described in Fig. 1B,

482   H corresponds to the thickness of the damage zone, which for mature strike-slip faults

483   is in the range of few hundreds of meters to few kilometers (Ben-Zion & Sammis, 2003;

484   Rockwell & Ben-Zion, 2007). Thus, the observations of Barka and Kadinsky-Cade (1988)

485   are consistent with our predictions. Moreover, our model predicts that the thicker the

486   damage zone the larger the offsets the earthquake can traverse.

5.2.3   *Variable stress conditions*

488   In the Earth's crust, the pre-stress along fault varies continuously due to tectonic

489   loading, spatially and temporally varying slip, and earthquake-induced Coulomb stress

490   transfer to and from neighboring faults. These processes increase or decrease pre-stress

491   magnitude and heterogeneity with time. For example, Mildon et al. (2019) showed that

492   the magnitude of pre-stress heterogeneity on faults in the Apennines exceeds 5 MPa, due

493   to cumulative addition of Coulomb stress transfer of known earthquakes from the last

494   660 years, and an additional strong pre-stress heterogeneous component arising from ir-

495 regular fault geometry, in particular from bends on faults, as discussed in the Section

496 5.2.1 above. Other works also find that pre-stress varies due to fault geometrical hetero-

497 geneities such as fault bends (e.g. Duan and Oglesby (2005)), fault roughness (e.g. Fang

498 & Dunham, 2013; Cattania & Segall, 2021), or fault segmentation (e.g. Harris et al. (2002)).

499 Examples of pre-stress variations unrelated to fault geometry include the 1966 Parkfield

500 earthquake arrest, attributed to a seismic velocity anomaly in the lower crust (Aki, 1979),

501 and pore pressure injections that may extend induced earthquake size (Galis et al., 2017).

502 On top of the initial variability in pre-stress, each subsequent rupture event further evolves

503 the pre-stress (Duan & Oglesby, 2005)).

504 Remarkably, the pulse equation (33) proposed in the present study allows for de-

505 ducing the initial stress at the interface from the final slip profile. As example, Fig. 9c

506 shows an application of equation (33) to slip data from the $M_w 7$ Ridgecrest earthquake

507 in 2019. As presented in the figure 2 of Chen et al. (2020), the rupture dynamics in the

508 later stage of the rupture becomes similar to the one-dimensional planar pulse discussed

509 in the present study. Therefore, we use the the profile of surface slip caused by the earth-

510 quake computed by Chen et al. (2020) using optical correlation of satellite images (shown

511 in the top panel of Fig. 9c) and plug it into our pulse equation (33) to get an estima-

512 tion of the stress profile before the rupture (shown in the bottom panel of Fig. 9c). The

513 section S.6 provides additional information on the slip inversion process and the param-

514 eters used to produce Fig. 9c.

5.3 Planar pulse versus circular crack

516 The one-dimensional pulse rupture discussed in the present study has some impor-

517 tant differences with the dynamics of circularly growing crack, each of them represent-

518 ing two end-member situations of the earthquake cycle: the circular crack model describes

519 the early stage of a seismic rupture (radial growth, rupture size much smaller than the

520 domain, unbounded available strain energy) whereas the planar pulse regime corresponds

521 to the advanced stage of the rupture (planar front, rupture size larger than the domain

522 dimensions H and W, limited available strain energy). Such a transition from crack to

523 pulse once the crack saturates the seismogenic layer, is observed to occur in large strike-

524 slip earthquakes, for example the 2019 $M_w 7.1$ Ridgecrest earthquake (Chen et al., 2020),

525 and the 2021 $M_w 7.4$ Madoi earthquake (Chen et al., 2022). Apart from stable pulse-like

526 solution discussed previously, planar rupture produces some interesting features of earth-

quake dynamics that remains debated in the circular-crack framework and could be explored in prospective works.

5.3.1 Stress drop

Using the pulse equation (33), the state of stress after the rupture can be predicted from the slip profile $\bar{u}_p$. As detailed in Eqs. (S.57)-(S.58), the stress drop in the one-dimensional model is given by $\eth\bar{\tau}_k$ or, in dimensional units,

$$\Delta\tau = \eth(\tau_0 - \mu_k\sigma_n), \tag{34}$$

Unlike circular cracks, planar pulse-like ruptures have then a stress drop independent of the rupture radius/size and proportional to the initial state of shear stress τ_0 acting on the fault before the event. Interestingly, this property of one-dimensional planar rupture implies that the final slip profile measured along fault zones after an earthquake provides information both on the initial shear stress before the rupture (as described in Figure 9c) but also after the rupture by subtracting the stress drop predicted in Eq. (34).

5.3.2 Back-propagating fronts at the arrest location

During the rupture arrests simulated in this paper, back-propagating fronts are sometimes observed after the sharp arrest of the main pulse front (e.g. by a stress or fracture energy barriers). As displayed in Figure S6, such fronts correspond to pulses of negative slip velocity that nucleate at the arrest location and propagate back to the nucleation zone. Back-propagating fronts are direct consequences of the stress drop described in Eq. (34) and the fact that one-dimensional planar rupture can reverse the sign of the shear stress along the interface. If the resulting negative shear stress is below the kinetic friction for negative slip (i.e. $\tau_0 - \Delta\tau < -\mu_k\sigma_n$), the interface is critically loaded and can host back-propagating fronts. Section S.7 and Figure S6 discuss how these secondary ruptures can be described by the same pulse theory presented in this paper and arise if the initial shear stress satisfies the following criterion:

$$\tau_0 > \frac{\eth+1}{\eth-1}\mu_k\sigma_n \geq 3\mu_k\sigma_n. \tag{35}$$

Recently, Idini and Ampuero (2020) reported travelling back-propagating fronts in numerical simulations of earthquake cycles within a low-velocity fault zone and discuss how recent progress in seismic monitoring allowed to detect secondary rupture fronts propagating with a reverse slip direction compared to the main rupture event. The presence

541 of this low-velocity fault core (as shown in Fig. 1) and the pulse-like nature of these back-

542 propagating fronts suggest some direct analogies with the response of our one-dimensional

543 model.

5.3.3 Triangular slip profile

545 Slip profiles of faults and earthquakes often display a triangular shape (Manighetti

546 et al., 2001, 2004, 2005; Scholz, 2019). These profiles have been observed to have a char-

547 acteristic asymmetry, where the short edge of the triangle is usually closer to the hypocen-

548 ter of the earthquake, the position of the maximum slip position is not constant, and the

549 ratio between the two edges of the triangle varies among earthquakes (Manighetti et al.,

550 2005). So far only a few models have been proposed to explain this observation. Manighetti

551 et al. (2004) suggested that off-fault damage and plasticity account for the triangular

552 slip distribution. Because, the presence of damage decreases the elastic moduli, Cappa

553 et al. (2014) suggested that the moduli of the off-fault damaged zone varies along the

554 fault. They demonstrated that this variation produces a triangular profile. In fact, this

555 variation of moduli will produce a variation in available strain energy stored along the

556 fault, and therefore this is equivalent to the slip pulse evolution when there is a deple-

557 tion of strain energy scenario, that we describe in Figs. 3D and 6. Thus, $\bar{\tau}_k$ in our model

558 encapsulates the backbone physics of the scenario of Manighetti et al. (2004) and Cappa

559 et al. (2014), yet offers a larger set of scenarios for obtaining triangular slip: any slip pulse

560 that propagates into regions of decreasing pre-stress or elastic strain energy will produce

561 such a profile. In fact, our work suggests that triangular slip profiles may be a signature

562 of pulse-like earthquakes that have been stopped by a depletion in available strain en-

563 ergy, which translates into depletion in $\bar{\tau}_k$.

6 Conclusion

565 To study frictional rupture arrest, we present a one-dimensional model that brings

566 a characteristic length scale H to the standard Burridge-Knopoff model and bridges it

567 to continuum fault models. The model captures the two types of boundary conditions

568 relevant at the early and late stage of earthquake rupture and reveals their fundamen-

569 tal impact on the style of the rupture (crack versus pulse), its energy balance, and the

570 arrest conditions. Under imposed-displacement boundary conditions, the proposed one-

571 dimensional model provides a good approximation for the dynamics of large earthquake

ruptures that saturate the width of the seismogenic zone and propagate as planar front (as sketched in Figure 1). In this context, the main conclusions are:

- The formulation of the model is minimal and generic and allows to wrap various earthquake arrest scenarios into the variations of two dimensionless variables $\bar{\tau}_k$ (initial pre-stress on the fault) and $\bar{d}_c$ (fracture energy).

- Using these two parameters, we propose simple scaling relationships to characterize the arrest length of earthquakes.

- The stress drop is directly proportional to the initial pre-stress.

- The regions of the fault that will arrest the next large earthquake can be predicted independently of where the rupture will nucleate.

- The transition from circular crack growth to the propagation of planar pulse brings new insight on unsettled features of natural earthquakes such as the observed asymmetric, triangular, slip profile along fault zones, the conditions for back-propagating ruptures, and the prevalence of the pulse-like rupture style for large earthquakes.

- The present paper focuses on earthquake dynamics, but the generality of the proposed one-dimensionless formulation may find applications in other geological settings where the size of the rupture exceeds the width of the surrounding bulk, such as landslides, glacier surge, and snow avalanches (Thøgersen, Gilbert, et al., 2019; Trottet et al., 2022).

Acknowledgments

598 **List of main symbols**

$\bar{x}$	Position along the fault
$\bar{t}$	Time
$\bar{u}$	Slip
$\bar{\tau}$	Shear stress
$\bar{\tau}_f$	Frictional stress
$\bar{\Gamma}$	Boundary conditions: imposed-stress ($\Gamma = 0$) or imposed-displacement ($\Gamma = 1$)
$\bar{\gamma}$	Elastic modulus parameter
$\bar{\tau}_k$	Pre-stress
$\bar{d}_c$	Critical weakening distance
$\bar{G}_c = \bar{d}_c/2$	Fracture energy
$\bar{K}$	One-dimensional stress intensity factor
$\bar{W}_b$	Breakdown work
$\bar{E}_{\mathrm{el}}$	Elastic energy
$\bar{E}_{\mathrm{kin}}$	Kinetic energy
$\bar{W}_{\mathrm{ext}}$	External work
$\bar{v}_c$	Rupture propagation speed
$\bar{u}_p$	Final slip (i.e. after rupture arrest)
$\bar{\beta}$	Numerical damping
$\bar{\mathcal{L}}$	Length of the domain
$\bar{L}$	Rupture length
$\bar{L}_{\mathrm{arr}}$	Arrest length
x	Position
t	Time
u_i	Displacement
$\hat{u}_0$	Imposed displacement at the top boundary
$\langle u_i \rangle$	Average displacement over the block height
σ_{ij}	Cauchy stress tensor
σ_n	Normal stress at the interface
τ_f	Frictional (shear) stress at the interface
H	Height of the solid block
λ	Lamé first coefficient
$\mathcal{G}$	Shear modulus
ρ	Solid density
μ_s	Static friction coefficient
μ_k	Dynamic friction coefficient
d_c	Critical slip weakening distance

Table 1.   List of variables used in the manuscript and the Supplementary Information. The dashed line separates the dimensionless variables (above) and the variables with dimensions (below). See also Table S1 for further information on how to relate these variables to dimensional quantities.

References

Abercrombie, R. E., & Rice, J. R. (2005). Can observations of earthquake scaling constrain slip weakening? *Geophysical Journal International*, *162*(2), 406–424.

Agliardi, F., Scuderi, M. M., Fusi, N., & Collettini, C. (2020). Slow-to-fast transition of giant creeping rockslides modulated by undrained loading in basal shear zones. *Nature communications*, *11*(1), 1–11.

Aki, K. (1979). Characterization of barriers on an earthquake fault. *Journal of Geophysical Research: Solid Earth*, *84*(B11), 6140–6148.

Amundsen, D. S., Scheibert, J., Thøgersen, K., Trømborg, J., & Malthe-Sørenssen, A. (2012). 1D Model of Precursors to Frictional Stick-Slip Motion Allowing for Robust Comparison with Experiments. *Tribology Letters*, *45*(2), 357–369. doi: 10.1007/s11249-011-9894-3

Barka, A., & Kadinsky-Cade, K. (1988). Strike-slip fault geometry in turkey and its influence on earthquake activity. *Tectonics*, *7*(3), 663–684.

Barras, F., Aldam, M., Roch, T., Brener, E. A., Bouchbinder, E., & Molinari, J.-F. (2020). The emergence of crack-like behavior of frictional rupture: Edge singularity and energy balance. *Earth and Planetary Science Letters*, *531*, 115978. doi: 10.1016/j.epsl.2019.115978

Bayart, E., Svetlizky, I., & Fineberg, J. (2016). Fracture mechanics determine the lengths of interface ruptures that mediate frictional motion. *Nature Physics*, *12*(2), 166–170. doi: 10.1038/nphys3539

Ben-Zion, Y., & Sammis, C. G. (2003). Characterization of fault zones. *Pure and applied geophysics*, *160*(3), 677–715.

Brantut, N., Garagash, D. I., & Noda, H. (2019). Stability of Pulse-Like Earthquake Ruptures. *Journal of Geophysical Research: Solid Earth*, *124*(8), 8998–9020. doi: 10.1029/2019JB017926

Braun, O. M., Barel, I., & Urbakh, M. (2009). Dynamics of Transition from Static to Kinetic Friction. *Physical Review Letters*, *103*(19), 194301. doi: 10.1103/PhysRevLett.103.194301

Brener, E. A., Aldam, M., Barras, F., Molinari, J.-F., & Bouchbinder, E. (2018). Unstable Slip Pulses and Earthquake Nucleation as a Nonequilibrium First-Order Phase Transition. *Physical Review Letters*, *121*(23), 234302. doi: 10.1103/PhysRevLett.121.234302

Brener, E. A., & Bouchbinder, E. (2021). Unconventional singularities and energy balance in frictional rupture. *Nature Communications*, *12*(1), 2585. doi: 10 .1038/s41467-021-22806-9

Brown, S. R., Scholz, C. H., & Rundle, J. B. (1991). A simplified spring-block model of earthquakes. *Geophysical Research Letters*, *18*(2), 215–218. doi: 10.1029/ 91GL00210

Burridge, R., & Halliday, G. (1971). Dynamic shear cracks with friction as models for shallow focus earthquakes. *Geophysical Journal International*, *25*(1-3), 261–283.

Burridge, R., & Knopoff, L. (1967). Model and theoretical seismicity. *Bulletin of the Seismological Society of America*, *57*(3), 341-371. Retrieved from `https://doi .org/10.1785/BSSA0570030341` doi: 10.1785/BSSA0570030341

Cappa, F., Perrin, C., Manighetti, I., & Delor, E. (2014). Off-fault long-term damage: A condition to account for generic, triangular earthquake slip profiles. *Geochemistry, Geophysics, Geosystems*, *15*(4), 1476-1493.

Carlson, J. M., Langer, J. S., & Shaw, B. E. (1994). Dynamics of earthquake faults. *Reviews of Modern Physics*, *66*(2), 657–670. doi: 10.1103/ RevModPhys.66.657

Cattania, C., & Segall, P. (2021). Precursory Slow Slip and Foreshocks on Rough Faults. *Journal of Geophysical Research: Solid Earth*, *126*(4), e2020JB020430. doi: 10.1029/2020JB020430

Chen, K., Avouac, J.-P., Aati, S., Milliner, C., Zheng, F., & Shi, C. (2020, January). Cascading and pulse-like ruptures during the 2019 Ridgecrest earthquakes in the Eastern California Shear Zone. *Nature Communications*, *11*(1), 22. doi: 10.1038/s41467-019-13750-w

Chen, K., Avouac, J.-P., Geng, J., Liang, C., Zhang, Z., Li, Z., & Zhang, S. (2022). The 2021 mw 7.4 madoi earthquake: An archetype bilateral slip-pulse rupture arrested at a splay fault. *Geophysical Research Letters*, *49*(2), e2021GL095243.

Cromer, A. (1981). Stable solutions using the Euler approximation. *American Journal of Physics*, *49*(5), 455–459. doi: 10.1119/1.12478

Das, S., & Aki, K. (1977). Fault plane with barriers: a versatile earthquake model. *Journal of Geophysical Research*, *82*(36), 5658–5670.

Day, S. M. (1982). Three-dimensional finite difference simulation of fault dynamics: Rectangular faults with fixed rupture velocity. *Bulletin of the Seismological Society of America*, *72*(3), 705–727. doi: 10.1785/BSSA0720030705

Duan, B., & Oglesby, D. D. (2005). Multicycle dynamics of nonplanar strike-slip faults. *Journal of Geophysical Research: Solid Earth*, *110*(B3).

Elbanna, A. E., & Heaton, T. H. (2012). A new paradigm for simulating pulse-like ruptures: the pulse energy equation. *Geophysical Journal International*, *189*(3), 1797–1806.

Elliott, A. J., Oskin, M. E., Liu-Zeng, J., & Shao, Y. (2015). Rupture termination at restraining bends: The last great earthquake on the altyn tagh fault. *Geophysical Research Letters*, *42*(7), 2164–2170.

Fang, Z., & Dunham, E. M. (2013). Additional shear resistance from fault roughness and stress levels on geometrically complex faults. *Journal of Geophysical Research: Solid Earth*, *118*(7), 3642–3654. doi: 10.1002/jgrb.50262

Freund, L. B. (1998). *Dynamic fracture mechanics*. Cambridge university press.

Gabriel, A.-A., Ampuero, J.-P., Dalguer, L. A., & Mai, P. M. (2012). The transition of dynamic rupture styles in elastic media under velocity-weakening friction. *Journal of Geophysical Research: Solid Earth*, *117*(B9).

Galis, M., Ampuero, J. P., Mai, P. M., & Cappa, F. (2017). Induced seismicity provides insight into why earthquake ruptures stop. *Science advances*, *3*(12), eaap7528.

Gvirtzman, S., & Fineberg, J. (2021). Nucleation fronts ignite the interface rupture that initiates frictional motion. *Nature Physics*, *17*(9), 1037–1042.

Harris, R. A., & Day, S. M. (1999). Dynamic 3d simulations of earthquakes on en echelon faults. *Geophysical Research Letters*, *26*(14), 2089–2092.

Harris, R. A., Dolan, J. F., Hartleb, R., & Day, S. M. (2002). The 1999 izmit, turkey, earthquake: A 3d dynamic stress transfer model of intraearthquake triggering. *Bulletin of the Seismological Society of America*, *92*(1), 245–255.

Heaton, T. H. (1990). Evidence for and implications of self-healing pulses of slip in earthquake rupture. *Physics of the Earth and Planetary Interiors*, *64*(1), 1–20. doi: 10.1016/0031-9201(90)90002-F

Husseini, M. I., Jovanovich, D. B., Randall, M., & Freund, L. (1975). The fracture energy of earthquakes. *Geophysical Journal International*, *43*(2), 367–385.

Ida, Y. (1972, July). Cohesive force across the tip of a longitudinal-shear crack and Griffith's specific surface energy. *Journal of Geophysical Research*, *77*(20), 3796–3805. doi: 10.1029/JB077i020p03796

Idini, B., & Ampuero, J.-P. (2020). Fault-Zone Damage Promotes Pulse-Like Rupture and Back-Propagating Fronts via Quasi-Static Effects. *Geophysical Research Letters*, *47*(23). doi: 10.1029/2020GL090736

Kammer, D. S., Radiguet, M., Ampuero, J.-P., & Molinari, J.-F. (2015). Linear Elastic Fracture Mechanics Predicts the Propagation Distance of Frictional Slip. *Tribology Letters*, *57*(3), 23. doi: 10.1007/s11249-014-0451-8

Ke, C.-Y., McLaskey, G. C., & Kammer, D. S. (2018). Rupture Termination in Laboratory-Generated Earthquakes. *Geophysical Research Letters*, *45*(23). doi: 10.1029/2018GL080492

Ke, C.-Y., McLaskey, G. C., & Kammer, D. S. (2022). Earthquake breakdown energy scaling despite constant fracture energy. *Nature Communications*, *13*(1), 1005. doi: 10.1038/s41467-022-28647-4

King, G., & Nábělek, J. (1985). Role of fault bends in the initiation and termination of earthquake rupture. *Science*, *228*(4702), 984–987.

Knopoff, L., & Ni, X. X. (2001). Numerical Instability at the Edge of a Dynamic Fracture. *Geophysical Journal International*, *147*(3), 1–6. doi: 10.1046/j.1365-246x.2001.01567.x

Kostrov, B. (1966). Unsteady propagation of longitudinal shear cracks. *Journal of Applied Mathematics and Mechanics*, *30*(6), 1241–1248.

Kostrov, B., & Das, S. (1988). *Principles of earthquake source mechanics*. Cambridge University Press.

Lambert, V., & Lapusta, N. (2020). Rupture-dependent breakdown energy in fault models with thermo-hydro-mechanical processes. *Solid Earth*, *11*(6), 2283–2302. doi: 10.5194/se-11-2283-2020

Lambert, V., Lapusta, N., & Perry, S. (2021). Propagation of large earthquakes as self-healing pulses or mild cracks. *Nature*, *591*(7849), 252–258. doi: 10.1038/s41586-021-03248-1

Lozos, J. C., Oglesby, D. D., Duan, B., & Wesnousky, S. G. (2011). The effects of double fault bends on rupture propagation: A geometrical parameter study. *Bulletin of the Seismological Society of America*, *101*(1), 385–398.

731 Madariaga, R. (1976). Dynamics of an expanding circular fault. *Bulletin of the Seis-*
732   *mological Society of America*, *66*(3), 639–666.

733 Magistrale, H., & Day, S. (1999). 3d simulations of multi-segment thrust fault rup-
734   ture. *Geophysical Research Letters*, *26*(14), 2093–2096.

735 Manighetti, I., Campillo, M., Sammis, C., Mai, P. M., & King, G. (2005). Evidence
736   for self-similar, triangular slip distributions on earthquakes: Implications for
737   earthquake and fault mechanics. *Journal of Geophysical Research: Solid Earth*,
738   *110*(B5).

739 Manighetti, I., King, G., Gaudemer, Y., Scholz, C., & Doubre, C. (2001). Slip ac-
740   cumulation and lateral propagation of active normal faults in afar. *Journal of*
741   *Geophysical Research: Solid Earth*, *106*(B7), 13667–13696.

742 Manighetti, I., King, G., & Sammis, C. G. (2004). The role of off-fault damage in
743   the evolution of normal faults. *Earth and Planetary Science Letters*, *217*(3-4),
744   399–408.

745 Manighetti, I., Zigone, D., Campillo, M., & Cotton, F. (2009). Self-similarity of the
746   largest-scale segmentation of the faults: Implications for earthquake behavior.
747   *Earth and Planetary Science Letters*, *288*(3-4), 370–381.

748 Marder, M. (1998). Adiabatic equation for cracks. *Philosophical Magazine B*, *78*(2),
749   203–214. doi: 10.1080/13642819808202942

750 Marone, C., & Scholz, C. (1988). The depth of seismic faulting and the upper transi-
751   tion from stable to unstable slip regimes. *Geophysical Research Letters*, *15*(6),
752   621–624.

753 Mildon, Z., Roberts, G. P., Walker, J. F., & Toda, S. (2019). Coulomb pre-stress
754   and fault bends are ignored yet vital factors for earthquake triggering and
755   hazard. *Nature communications*, *10*(1), 1–9.

756 Olami, Z., Feder, H. J. S., & Christensen, K. (1992). Self-organized criticality in a
757   continuous, nonconservative cellular automaton modeling earthquakes. *Physical*
758   *Review Letters*, *68*(8), 1244–1247. doi: 10.1103/PhysRevLett.68.1244

759 Paglialunga, F., Passelègue, F., Brantut, N., Barras, F., Lebihain, M., & Violay, M.
760   (2021). On the scale dependence in the dynamics of frictional rupture: Con-
761   stant fracture energy versus size-dependent breakdown work. *arXiv:2104.15103*
762   *[physics]*.

763 Palmer, A. C., & Rice, J. R. (1973). The growth of slip surfaces in the progressive

failure of over-consolidated clay. *Proceedings of the Royal Society of London. A. Mathematical and Physical Sciences*, *332*(1591), 527–548. doi: 10.1098/rspa.1973.0040

Perrin, C., Manighetti, I., Ampuero, J.-P., Cappa, F., & Gaudemer, Y. (2016). Location of largest earthquake slip and fast rupture controlled by along-strike change in fault structural maturity due to fault growth. *Journal of Geophysical Research: Solid Earth*, *121*(5), 3666–3685.

Roch, T., Brener, E. A., Molinari, J.-F., & Bouchbinder, E. (2022). Velocity-driven frictional sliding: Coarsening and steady-state pulses. *Journal of the Mechanics and Physics of Solids*, *158*, 104607. doi: 10.1016/j.jmps.2021.104607

Rockwell, T. K., & Ben-Zion, Y. (2007). High localization of primary slip zones in large earthquakes from paleoseismic trenches: Observations and implications for earthquake physics. *Journal of Geophysical Research: Solid Earth*, *112*(B10).

Scholz, C. H. (1998). Earthquakes and friction laws. *Nature*, *391*(6662), 37–42.

Scholz, C. H. (2019). *The Mechanics of Earthquakes and Faulting* (Third ed.). Cambridge University Press. doi: 10.1017/9781316681473

Sibson, R. H. (1985). Stopping of earthquake ruptures at dilational fault jogs. *Nature*, *316*(6025), 248–251.

Sibson, R. H., & Das, S. (1986). Rupture interaction with fault jogs. *Earthquake Source Mechanics*, *37*, 157–167.

Thøgersen, K., Aharonov, E., Barras, F., & Renard, F. (2021). Minimal model for the onset of slip pulses in frictional rupture. *Physical Review E*, *103*(5), 052802. doi: 10.1103/PhysRevE.103.052802

Thøgersen, K., Gilbert, A., Schuler, T. V., & Malthe-Sørenssen, A. (2019). Rate-and-state friction explains glacier surge propagation. *Nature Communications*, *10*(1), 2823. doi: 10.1038/s41467-019-10506-4

Thøgersen, K., Sveinsson, H., Scheibert, J., Renard, F., & Malthe-Sørenssen, A. (2019). The moment duration scaling relation for slow rupture arises from transient rupture speeds. *Geophysical Research Letters*, *46*(22), 12805–12814.

Tinti, E., Spudich, P., & Cocco, M. (2005). Earthquake fracture energy inferred from kinematic rupture models on extended faults. *Journal of Geophysical Research*, *110*(B12), B12303. doi: 10.1029/2005JB003644

Trømborg, J., Scheibert, J., Amundsen, D. S., Thøgersen, K., & Malthe-Sørenssen, A. (2011). Transition from Static to Kinetic Friction: Insights from a 2D Model. *Physical Review Letters*, *107*(7), 074301. doi: 10.1103/ PhysRevLett.107.074301

Trømborg, J., Sveinsson, H., Scheibert, J., Thøgersen, K., Amundsen, D. S., & Malthe-Sørenssen, A. (2014). Slow slip and the transition from fast to slow fronts in the rupture of frictional interfaces. *Proceedings of the National Academy of Sciences*, *111*(24), 8764–8769. doi: 10.1073/pnas.1321752111

Trottet, B., Simenhois, R., Bobillier, G., Bergfeld, B., van Herwijnen, A., Jiang, C., & Gaume, J. (2022). Transition from sub-Rayleigh anticrack to supershear crack propagation in snow avalanches. *Nature Physics*, *18*(9), 1094–1098. Retrieved from https://www.nature.com/articles/s41567-022-01662-4 doi: 10.1038/s41567-022-01662-4

Viesca, R. C., & Rice, J. R. (2012). Nucleation of slip-weakening rupture instability in landslides by localized increase of pore pressure. *Journal of Geophysical Research: Solid Earth*, *117*(B3). doi: 10.1029/2011JB008866

Weng, H., & Ampuero, J.-P. (2019). The Dynamics of Elongated Earthquake Ruptures. *Journal of Geophysical Research: Solid Earth*, *124*(8), 8584–8610. doi: 10.1029/2019JB017684

Wesnousky, S. G. (1988). Seismological and structural evolution of strike-slip faults. *Nature*, *335*(6188), 340–343.

Zheng, G., & Rice, J. R. (1998). Conditions under which velocity-weakening friction allows a self-healing versus a cracklike mode of rupture. *Bulletin of the Seismological Society of America*, *88*(6), 1466–1483. doi: 10.1785/BSSA0880061466